Tampere University

Lalit Pun

EFFECT OF SPECIMEN GEOMETRY AND FRICTION IN THE HIGH STRAIN RATE COMPRESSION TESTS

Faculty of Engineering and Natural Sciences
Master of Science
October 2019

ABSTRACT

Lalit Pun: Effect of specimen geometry and friction in the high strain rate compression tests
Master of Science
Tampere University
Master's degree programme in Materials Science and Engineering
October 2019

The Split Hopkinson pressure bar (SHPB) or Kolsky bar is widely used to characterize the mechanical behavior of materials at different strain rates and different temperatures. The proper characterization of mechanical behavior of different materials at different strain rates and temperatures requires minimization of potential errors that can occur due to different factors such as friction, improper selection of specimen geometry and size. In this study, the effect of lubrication, specimen geometry, and size on the dynamic behavior of aluminum alloy has been investigated experimentally and numerically.

Dynamic compressive tests were performed at different strain rates and at room temperature using the specimens made of aluminum alloy 7050-T351, with diameters of 5mm, 6mm, 8mm, 10mm and 12mm and different length to diameter ratios of 0.6, 1 and 1.4. The tests were performed using cylindrical specimens, but a few experiments were also carried out using the cuboid specimens to check the compatibility of the used specimens.

The shorter specimen of smaller diameter (5mm) was found to be sensitive to lubrication, but larger specimens did not show larger deviations in the results. The strain rates and calculated temperature rise in the specimens due to adiabatic heating decreased with the lubrication applied between the specimen and pressure bars. Also, the suitable specimen diameter and aspect ratios were identified for high strain rate compression tests. The aluminum alloy 7050-T351 showed the increased strain rate sensitivity above strain rates of 1000 s^{-1}. Moreover, the cuboid specimens should be discarded in the compression tests as they provide unreliable results.

The experimental results were fitted to the Johnson-Cook constitutive material model. The obtained parameters were then used in the numerical simulation where a replica of the test device used in the lab was constructed using a 2D-axisymmetric model in the y-axis. The effects of friction were also studied simulating the reflected and transmitted stress-waves using coefficients of friction ranging from 0-0.5. The results showed that the reflected stress-waves decrease slightly with the increase in friction, but the transmitted stress-waves increase significantly. The simulated yield stress also increases with increment in coefficient values of friction.

Keywords: Aluminum alloy 7050, friction, Split-Hopkinson pressure bar, high strain rate, Johnson-Cook, Numerical simulations

PREFACE

This work was done at Universidad Politécnica de Madrid during my Erasmus exchange studies. I would like to thank especially my supervisor, Dr. Francisco Galvez for providing this topic to start in understanding the dynamic behavior of materials. I truly appreciate his guidance in the class and laboratory. The acknowledgments are also extended to Dr. Mikko Hokka from Tampere University, Hervanta campus who has been an essential part of this thesis which would have been elusive without his valuable comments and suggestions.

Last but not least I would like to thank my family members back in Nepal for their continuous love and support.

Tampere, 24 October 2019

Lalit Pun

CONTENTS

LIST OF FIGURES

LIST OF TABLES

LIST OF SYMBOLS

a	Acceleration
b	Dislocation burger vector
c_0	Velocity of the longitudinal wave
C_p	Specific heat capacity
D	Diameter
e	Engineering strain
E	Young's modulus
F	Force
G	Amplifier gain
H(σ)	Activation energy
k	Boltzmann constant
K	Gage factor
L_s	Length of the specimen
m	Mass
Q_{JC}	Work hardening ratio
R_0	Electrical resistance
R_L	Longitudinal resistance
R_T	Transversal resistance
s	Engineering stress
T	Temperature
T_{melt}	Melting temperature
u(x)	Displacement at distance x
V	Voltage
v	Poisson's ratio
ρ	Density
σ	True stress
σ_{eff}	Effective stress
ε	True strain
ε_{eff}	Effective strain
ε_I	Incident strain
ε_R	Reflected strain
ε_T	Transmitted strain
τ	Shear stress
μ	Coefficient of friction
Ω	Ohms
γ	Shear strain
β	Taylor-Quinney coefficient

LIST OF ABBREVIATIONS

2D	Two-dimensional
AA	Aluminum alloy
ASB	Adiabatic shear bands
BCC	Body-centered cubic
CG	Conventional
ECAP	Equal channel angular processing
EOS	Equation of state
Eq.	Equation
FCC	Face-centered cubic
FE	Finite element
JC	Johnson-Cook
$\frac{L}{D}$	Length to diameter ratio
MTS	Mechanical threshold stress
OFHC	Oxygen-free high thermal conductivity
Q&T	Quenched & tempered
SHPB	Split-Hopkinson pressure bar
UFG	Ultrafine grained
ZA	Zerilli-Armstrong

1. INTRODUCTION

Classical theories of elasticity and plasticity only assume that the applied loads are static, and therefore the deformation of materials or structure is slow. On the other hand, it is well known that materials behavior at dynamic loading is quite different from static loading. Some examples of dynamic events are the collision of vehicles, explosions, birds' impact on aircraft, material forming, natural disasters such as earthquakes, tsunamis, floods and so on. The knowledge of material behaviors at those conditions is necessary. Various impact experiments have been designed to study the dynamic properties of various materials including metals, ceramics, polymers, composites, hybrid materials, etc. The Split Hopkinson bar, also known as the Kolsky bar is widely used to study the material properties up to strain rates of $10^4\ s^{-1}$. [1,2]

Aluminum alloy 7050-T351 is extensively used by automotive and aerospace industries mainly due to its attractive combination of strength and corrosion resistance properties [3, 4]. The strain rate sensitivity of pure conventional aluminum decreases with the increase in alloying contents and different heat treatment methods but regardless these alloys tend to exhibit more sensitivity at elevated temperatures [5,6]. Proper evaluation of the strain rate sensitivity and stress-strain response at various strain rates require minimization of errors during mechanical testing that can occur due to various factors such as friction and improper selection of specimen geometry and size.

The main purpose of this work is to investigate the effects of friction and determine the appropriate specimen diameter and length to diameter ratio for high strain rate compression tests of aluminum alloy 7050-T351. Dynamic compression tests were performed at room temperature using specimens with different diameters of 5mm, 6mm, 8mm,10mm and 12mm with different aspect ratios of 0.6, 1 and 1.4. The experimental data were fitted to the Johnson-Cook constitutive model and numerical simulations were carried out in LS-Dyna using the 2D-axisymmetric model.

A brief literature review related to this work is presented in the following sections. This includes a short description of the stress waves in solids, their types and wave interaction. Then, a brief history of the high strain rate testing, description of split Hopkinson bar apparatus and ways to analyze the experimental data are also presented. The properties of materials at high strain rate and mechanism associated with the observed behavior is also discussed along with the high strain rate behavior of aluminum alloys. Also, a review of the currently used Johnson-Cook constitutive model is also provided.

1.1 Stress Waves in Solids

The disturbance to the mechanical equilibrium in a deformable solid medium by the application of external force is represented by the change in particle velocity and the corresponding changes in stress and strain states. Initially, some parts of a solid are disturbed and some finite time durations are required for the disturbance to be felt by other parts of the body. These kinds of waves propagation which causes deformation in the material termed as stress waves. These stress waves can be created by different sources, for example, an impact between two materials, explosions, etc. When the amplitude of the produced stress waves is less than the yield strength of the material, the waves are called elastic waves whereas, when the amplitude of the stress waves surpasses the yield strength of the material, the waves cause plastic or permanent deformation. [7-9]

Depending on the motion of particles and direction of propagation of the waves as well as the boundary conditions, different kinds of elastic waves can propagate in the solids. The most general types of elastic waves in the solids are [7,8]:

- Transverse waves
- Longitudinal waves
- Interfacial waves
- Surface waves
- Bending waves

1.1.1 Elastic Wave in a Cylindrical Bar

If we consider a uniform circular long bar made of isotropic material as shown in Figure 1a, a compressive stress wave is produced in the bar upon the impact of the striker bar that travels from left to right. Let u(x) be the displacement of plane AB in the bar which is at distance x. Then u+ $\frac{\partial u}{\partial x}\delta x$ is the displacement of plane A'B' at the distance x+δx from the origin.

(a)

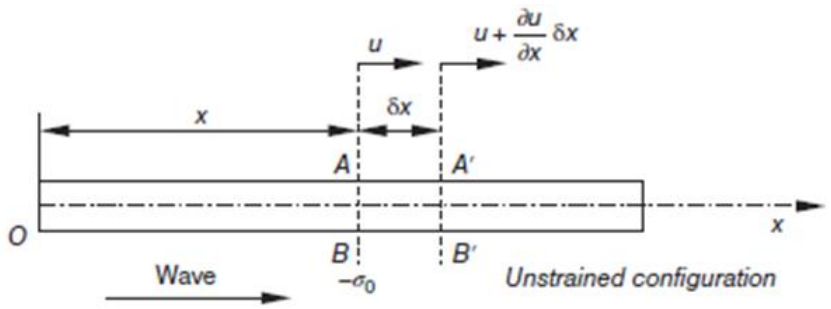

(b)

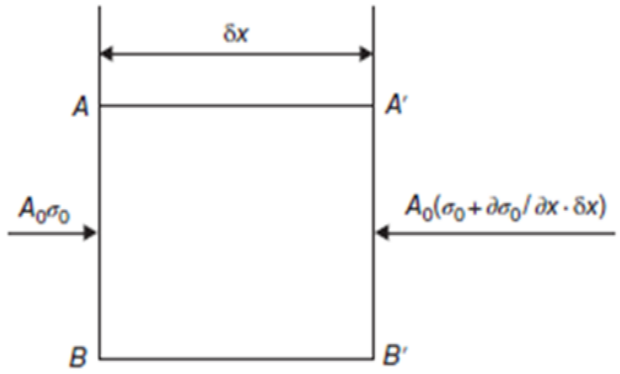

***Figure 1**: (a) The propagation of the compressive elastic wave in a uniform circular bar and (b) the equilibrium of a representative element of the bar [7]*

The representative element of the bar is illustrated in Figure 1b. Here, A_0 is the initial area of the bar, ρ_0 is the initial density of the bar material and σ_0 is the stress transmitted after the impact. Applying Newton's second law to AA'BB' we obtain:

$$F = ma$$

$$\frac{\partial \sigma_0}{\partial x}\delta x A_0 = \rho_0 A_0 \delta x \frac{\partial^2 u}{\partial t^2} \tag{1.1}$$

$$\frac{\partial \sigma_0}{\partial x} = \rho_0 \frac{\partial^2 u}{\partial t^2} \tag{1.2}$$

The strain of the element is

$$\varepsilon = \frac{\partial u}{\partial x}$$

And, the deformation is supposed to be elastic and then, according to Hooke's law,

$$\sigma_0 = E\frac{\partial u}{\partial x} \tag{1.3}$$

Thus,

$$\frac{\partial}{\partial x}\left[E\frac{\partial u}{\partial x}\right] = \rho_0 \frac{\partial^2 u}{\partial t^2} \tag{1.4}$$

And,

$$\frac{\partial^2 u}{\partial t^2} = \frac{E}{\rho_0}\frac{\partial^2 u}{\partial x^2} \tag{1.5}$$

Equation (1.5) is the differential equation for typical one-dimensional wave and the velocity of this wave (c_0) is given by

$$c_0 = \sqrt{\frac{E}{\rho_0}} \tag{1.6}$$

The speed of longitudinal waves in three typical materials is given in Table 1. It can be noticed that the wave speed depends on both Young's modulus and density of the material.

Table 1: *Typical longitudinal wave speed in solid materials* [8]

	Steel	**Aluminum**	**Glass**
E(Gpa)	205	75	95
$\rho_0(g/cm^3)$	7.8	2.7	2.5
c_0(m/s)	5100	5300	6200

When the waves encounter a boundary, they are reflected as well as refracted at the boundary. This means that the incident wave is reflected as well as transmitted at the interface of two materials as seen in Figure 2. This phenomenon occurs when the wave encounters a medium having a different mechanical impedance which is defined as the product of the medium density and its elastic wave speed. Furthermore, the sum of the reflected wave and transmitted wave should always be equal to the incident wave. [7,8]

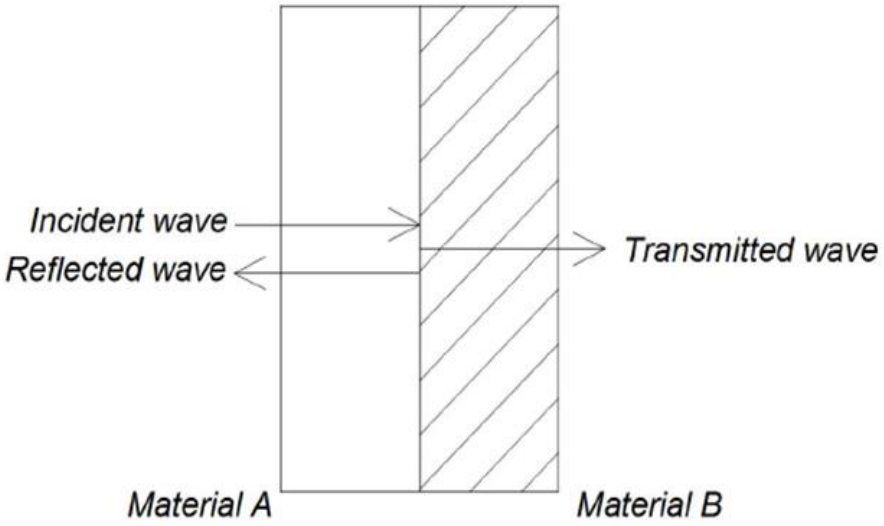

***Figure 2**: Incident wave reflected and transmitted at the boundary [9]*

1.2 High Strain Rate Testing

High strain rate testing is often needed for structural applications and metalworking operations. Critical structures that are built should always be tested to ensure its functionality during dynamic events and at different ranges of temperatures. Similarly, materials in metalworking operations encounter various temperatures and strain rates. Therefore, knowledge of the materials' behavior at material forming operations such as rolling, drilling, stamping, cold -drawing, etc. and structural impacts such as bird impact and loading at high velocities such as those occurring during an earthquake are needed. Figure 3 summarizes the different kinds of instruments that can be used for material testing at different strain rates. Conventional servo-hydraulic machines are used for quasi-static tests up to strain rates of 1 s^{-1}. Hopkinson bar techniques (up to 10^4 s^{-1}) and light gas gun or explosively driven plate impact (10^4-10^6 s^{-1}) can be used for testing at higher strain rates. [10]

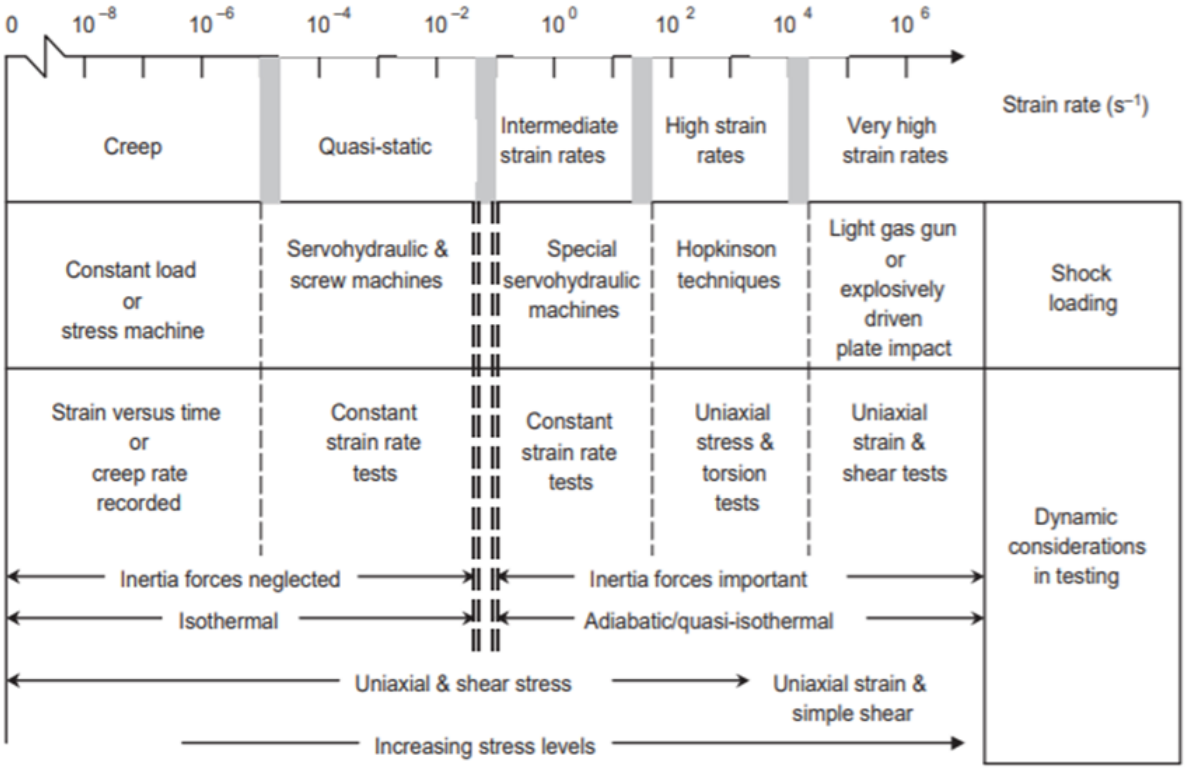

Figure 3:*Various kinds of instruments for materials testing at different strain rates [10]*

The Hopkinson bar method was originally invented by John Hopkinson [11] and his son, Bertram Hopkinson [12,13]. Bertram Hopkinson [13] developed a method to measure the pressure and their time period produced by rifle bullet or high explosives. He used a cylindrical pressure bar made of steel which was suspended as shown in Figure 4.

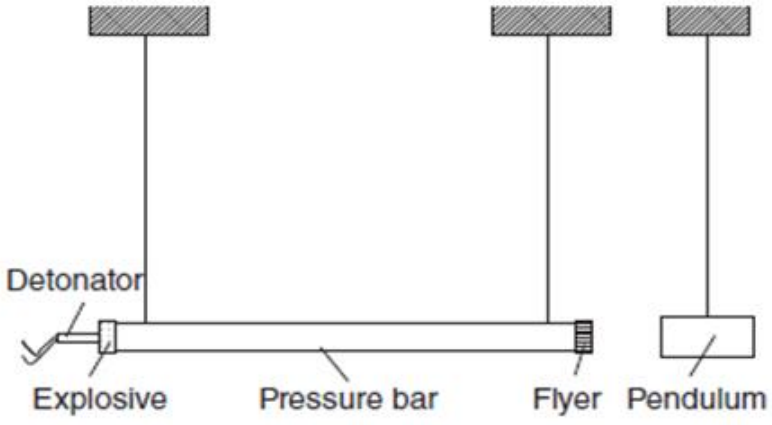

Figure 4: *Bertram Hopkinson experimental device [8]*

It was not easy to measure the stress wave produced during the experiments as there were no sophisticated instruments such as strain gage or high-speed camera like

nowadays. A flyer was attached to the end of the rod by oil and an explosion was carried out at the left end of the pressure bar. After the explosion, a compressional pulse propagates in the pressure bar which shifts forward. The compression pulse is then reflected as soon as it reaches the free end of the bar and as a result of reflected tensile pulse, the flyer falls off. Then, a pendulum is hanged distinctly next to a pressure bar that is intruded by the fallen flyer. The initial velocity and the initial momentum of the flyer can be estimated by calculating the swing of the pendulum. Although Hopkinson's original method has the advantage of simplicity, it had some difficulties which were later improved by Davies [14] and Kolsky [15]. They basically used two pressure bars in series and the sample is allocated in between the bars. This technique, therefore, is known as either a split-Hopkinson pressure bar, Davies bar or Kolsky bar.

1.2.1 Split-Hopkinson Pressure Bar (SHPB) in Compression

There is no universal standard design for the SHPB test apparatus and the most commonly used configuration which is similar to that used by Kolsky [15], is shown in Figure 5a. The compression Hopkinson bar test apparatus consists of the following:

- 2 long symmetrical bars and projectile which mostly is shorter than the bars
- Gas gun tube or alternative propulsion gear to launch the projectile
- Alignment fixtures that allow the projectile and pressure bars to move freely in the axial direction during the tests
- Strain gages fitted on both incident and transmitted bar for the measurement of the stress waves in the bars
- Data acquisition system to record the stress-waves in the bars

(a)

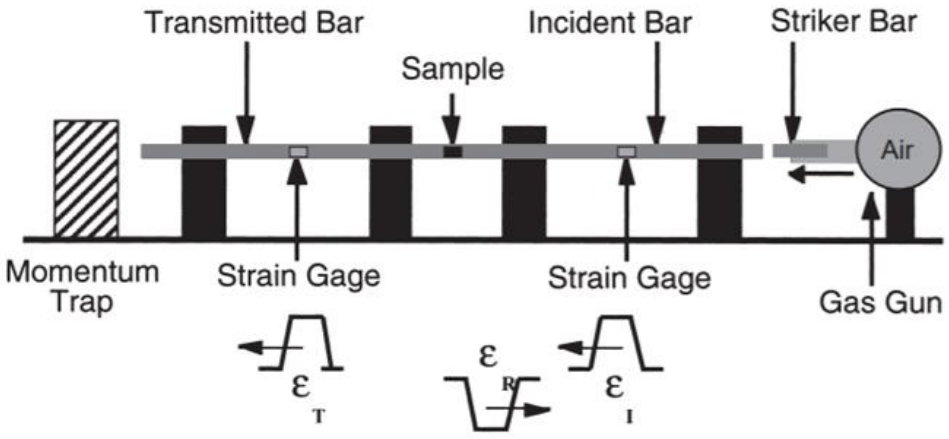

(b)

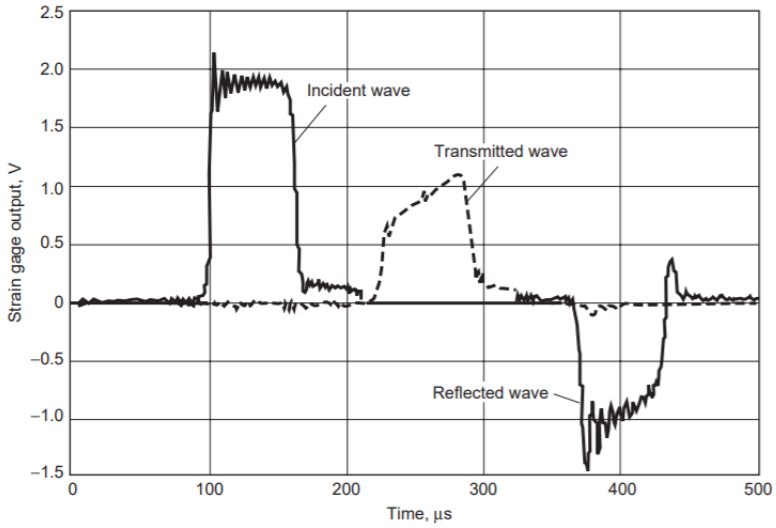

Figure 5: *Split Hopkinson pressure bar. (a) Experimental test arrangement; (b) Strain gage output from the experiment [16]*

The projectile is fired with the help of a gas gun at the end of the bar commonly known as the incident bar. The sample is simply sandwiched between the incident and the transmitted bars (Figure 5a). Typically, high strength structural steel, maraging steel or nickel alloy such as Inconel is used for the construction of the bars because the maximum stress that can be achieved within the deforming specimen depends on the yield strength of the bar materials that have been used. Basically, the bars should remain elastic during the experiments. [16]

To validate the test, the diameter and length of the pressure bars are to be chosen in such a way that only one-dimensional wave is propagated in the bars. Moreover, the ratio of length to diameter (L/D) should be around 20 for each bar to separate the recorded incident and reflected waves. Also, higher strain rate experiments can be obtained with the bars of the smallest diameter. In order to avoid the interference of the waves, the bars should be constructed in such a way that it is at least twice as long as the incident compression wave. [16]

The incident compression wave can be generated by striking the projectile at the end of the incident bar. The velocity of the projectile can be chosen accordingly to achieve desired strain rates. Some part of the incident wave is reflected on reaching the bar-specimen boundary whereas the remaining of the wave passes through the transmitted bar, known as the transmitted wave. These stress waves are then recorded by the strain gages normally mounted on the middle section of both incident and transmitted bars. Figure 5b shows the strain gage output recorded as a function of time for all the three

stress-waves measured during the experiment. The recordings obtained from the strain gages then can be analyzed to construct the strain rate, the force transmitted in the specimen and the stress-strain response of the tested specimen. These data are also important in numerical modeling. [16]

1.2.2 Analysis of the Split-Hopkinson Pressure Bar

According to the uniaxial elastic wave propagation theory, it is assumed that the stress-waves are known in every point of the Hopkinson pressure bar as an elastic wave can be relocated to any points without scattering. So, the force transmitted, and velocity of the specimen can be obtained by shifting the transmitted wave to the specimen-bar interface. In a similar way, incident and reflected waves can be shifted to determine the incident force and velocity. [8,16]

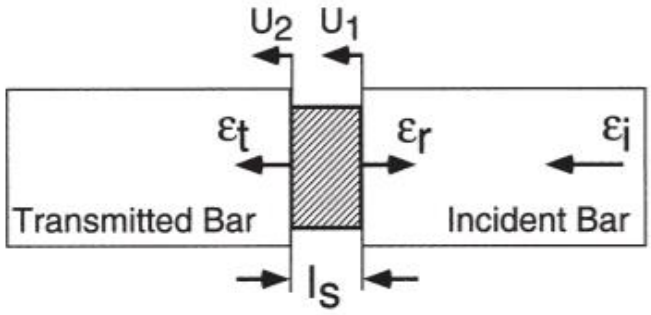

Figure 6: *Enlarged view of the incident(input) bar/specimen/ transmitted (output) bar region [16]*

The strains in the bars are represented by ε_I, ε_R and ε_T (incident, reflected, and transmitted strains) respectively as shown schematically in the enlarged view of the test specimen in Figure 6. Also in Figure 6, U_1 and U_2 refer to the particle velocities at the incident and transmitted bars respectively and l_s is the length of the specimen. So, the forces and velocities of the specimen can be calculated by the following Equations:

$$F_{incident} = EA_B(\varepsilon_I + \varepsilon_R) \tag{1.7}$$

$$F_{output} = EA_B\varepsilon_T \tag{1.8}$$

$$V_{incident} = c_0(\varepsilon_I - \varepsilon_R) \tag{1.9}$$

$$V_{output} = c_o\,\varepsilon_T \tag{1.10}$$

where $F_{incident}$, F_{output}, $V_{incident}$, V_{output} are the forces and the particle velocities at the incident and transmitted bars respectively; A_B, E, and c_o are the cross-sectional area of the bars, Young's modulus, and the longitudinal wave velocity respectively.

The compressional strain rate $\dot{\varepsilon_s}$ can be determined by the difference in velocities at both ends of the specimen;

$$\dot{\varepsilon_s} = \frac{V_{output} - V_{incident}}{L_s} \tag{1.11}$$

Then, the stress in the specimen is,

$$\sigma_s = \frac{F_{output}}{A_s} \tag{1.12}$$

where L_s and A_s are the length and cross-sectional area of the specimen respectively.

Assuming uniform deformation, the strains in the specimen state can be written as: ε_I+ε_R=ε_T. By substituting Eq. (1.9) into Eq. (1.11), the strain rate of the specimen can be calculated,

$$\dot{\varepsilon_s} = \frac{2c_o}{L_s}\varepsilon_R \tag{1.13}$$

The strain of the specimen then can be calculated by integrating the strain rate over time;

$$\varepsilon_s = \frac{2c_o}{L_s}\int_0^t \varepsilon_R \, dt \tag{1.14}$$

Then, the stress of the specimen can be calculated by;

$$\sigma_s = \frac{E\,A_B}{A_s}\varepsilon_T \tag{1.15}$$

The engineering stress and strain of the specimen obtained from Equations (1.14-1.15), and this analysis is termed as one-wave equations of the SHPB because it uses only the reflected wave to calculate strain and only transmitted wave is used to calculate strain in the sample [8,16].

At the early stages of the dynamic experiment, the load is introduced only at one end of the specimen while the other end remains static. So, over the years, several authors [17-19] have proposed a three-wave analysis in order to use the average of the two forces to calculate the stresses instead of Eq. (1.12):

$$\sigma_s = \frac{F_{incident+}\ F_{output}}{2A_s} \tag{1.16}$$

Accordingly, other equations for three-wave SHPB can be derived;

$$\sigma_s = \frac{E\ A_B}{2A_s}(\varepsilon_I + \varepsilon_R + \varepsilon_T) \tag{1.17}$$

$$\dot{\varepsilon_s} = \frac{c_o}{L_s}(\varepsilon_R + \varepsilon_T - \varepsilon_I) \tag{1.18}$$

$$\varepsilon_s = \frac{c_o}{L_s}\int_0^t (\varepsilon_R + \varepsilon_T - \varepsilon_I)\ dt \tag{1.19}$$

1.2.3 Tensile Split-Hopkinson Pressure Bar

Some materials like cast iron and fiber-reinforced composites have different tensile and compressive properties. Moreover, the properties of fibers can only be evaluated in tension. For this reason, the tensile version of a split-Hopkinson bar is required. Figure 7 [16] shows a schematic picture of a tensile SHPB setup. The principles and data analysis techniques for the tensile split-Hopkinson pressure bar are similar to those discussed above for compression SHPB. The main differences are the specimen geometry, methods of generating tensile loading pulse and arrangement of the specimen between the incident and transmitted bars. Different types of tension SHPB have been developed to study the dynamic response of the materials in tension, and three common types are presented here. [17,20-22]

***Method 1**:* The first method developed by Lindholm and Yeakley [20] consists of a solid incident bar while the transmitted bar is made of a hollow tube. Hat shaped specimen is sandwiched between the bar and the tube. The compressive waves in the incident bar generate the tensile load in the specimen. The main advantage of this method is that when a hollow transmitted bar matches the incident bar, tensile experiments can be performed using a standard compressive SHPB loading [16].

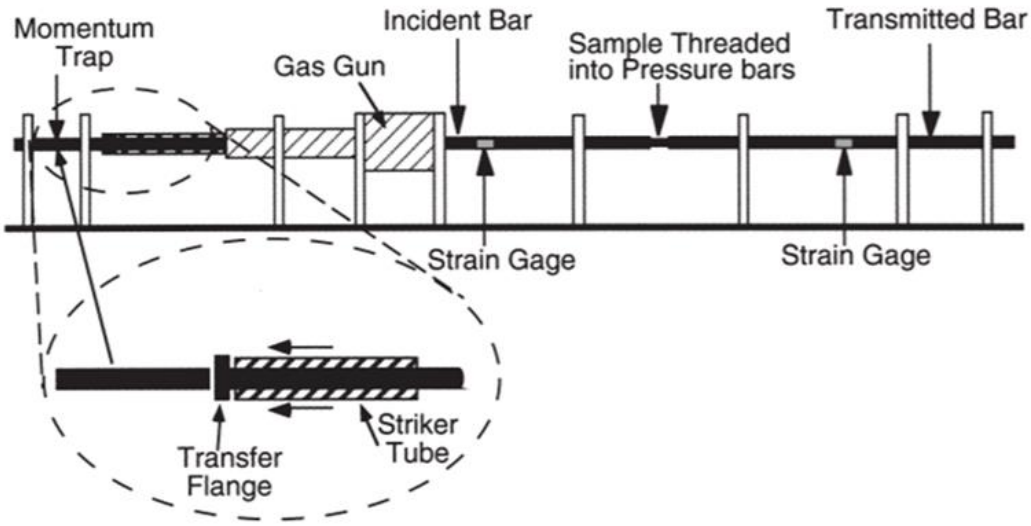

Figure 7: *Schematic of a tensile split-Hopkinson pressure bar test [16]*

Method 2**:** In this method, the specimen is subjected to uniaxial tensile stress using an axisymmetric circular or flat sheet tension specimen attached directly into the ends of the incident and transmitted bars. A tensile pulse in the experiment can be generated by directly impacting the striker tube at the end of the incident bar.[21]

Method 3: In this type of tensile Hopkinson bar loading method, a circular specimen is placed onto the ends of the incident and transmitted bars. The sample is protected by a circular collar from initial compression pulses and loaded in tension by the reflection of the compressive pulses produced at the free end of the transmitted bar. [22]

1.3 High Strain Rate Properties of Materials

Bertram Hopkinson in 1905 [12] performed high strain rate experiments on steel wires and he found out that the strength of steel at high strain rate was at least twice its strength at lower strain rate. The experiments demonstrated that the steel wires become brittle at higher strain rates. Afterward, the high strain rate behavior of many materials including, metals, polymers, composites, ceramics, soft materials, and so on have been studied extensively. Plastic deformation of materials at high strain rate can be described by the constitutive equations that associate effective stress σ with strain ε, strain rate $\dot{\varepsilon}$, and temperature T [7]. This can be demonstrated by:

$$\sigma = f(\varepsilon, \dot{\varepsilon}, T) \tag{1.20}$$

Since the plastic deformation process is not reversible and it also depends on the path, the response of the material at a certain point also depends on the deformation

substructures along with the current stress-strain state. So, for that reason, we need to sum the general term called 'deformation history' to the above Equation (1.20). [7]

$$\sigma = f(\varepsilon, \dot{\varepsilon}, T, deformation\ history) \tag{1.21}$$

It is well known that both the stress and strain are second-order tensors each with 6 different components and the constitutive equations can be represented in scalar form rather than in tensor form by calculating the effective stress σ_{eff} and effective strain ε_{eff} using the following equations:

$$\sigma_{eff} = \frac{1}{\sqrt{2}}\sqrt{(\sigma_1 - \sigma_2)^2 + (\sigma_2 - \sigma_3)^2 + (\sigma_3 - \sigma_1)^2} \tag{1.22}$$

$$\varepsilon_{eff} = \frac{\sqrt{2}}{3}\sqrt{(\varepsilon_1 - \varepsilon_2)^2 + (\varepsilon_2 - \varepsilon_3)^2 + (\varepsilon_3 - \varepsilon_1)^2} \tag{1.23}$$

Here in Equations (1.22) - (1.23) σ_1, σ_2, σ_3 and ε_1, ε_2, ε_3 are the principal stresses and strains respectively.

Similarly, we can also calculate effective shear stress in order to formulate the constitutive equations as shear stresses. In fact, shear stresses are more influential components in the plastic deformation of materials. [7]

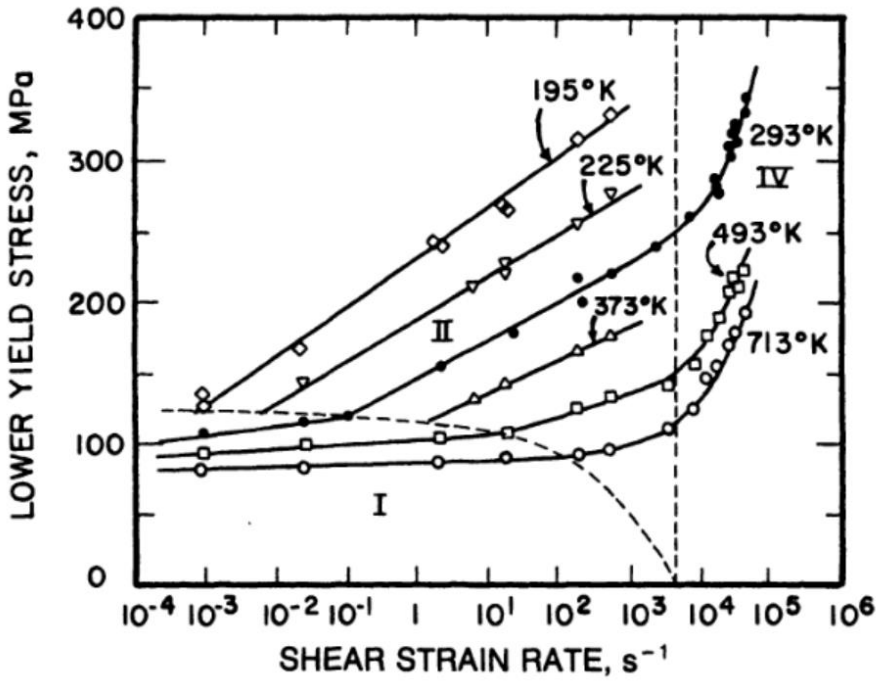

***Figure 8**: Lower yield stress vs strain rate for a mild steel [7]*

Figure 8 represents the lower yield strength of mild steel plotted against the logarithm of the strain rate at different temperatures. It can be clearly seen that the yield stress decreases with the increase in temperature. Moreover, for the strain rates lower than 10^3 s^{-1}, yield stress changes comparatively slowly with strain rate, whereas for the strain rates greater than 10^3 s^{-1}, the yield stress alters swiftly. Hence, it can be concluded that for mild steel, increment in strain rates tends to increase the yield stress values and this phenomenon of increasing yield stress with strain rate is more pronounced at lower temperatures.

In the following paragraphs, dynamic compressive, tensile and shear mechanical properties of common metals like bainitic steel, martensitic steel, aluminum alloy, etc. are discussed briefly just to remind that the materials behave differently at high strain rates as compared to static conditions. The high strain rate behavior of aluminum alloys and the mechanism associated with the observed behavior are discussed in detail in section 1.4.

The effects of strain rate and temperature on the compressive flow stress of 2519A aluminum alloy have been analyzed by Wen-hui et al. [23] using cylindrical specimens. The quasi-static tests were performed at strain rates of 0.001,0.01 and 0.1 s^{-1} and dynamic experiments were conducted under different strain rates ranging from 1500- 8300 s^{-1} at different temperatures. The plot of the experimental results at room temperature is shown below in Figure 9. The yield stress measured at room temperature increases with an increase in strain rates. Also, when comparing the quasi-static tests with the dynamic tests, instability near yield point can be seen with higher strain rates but they become stable after plastic deformation.

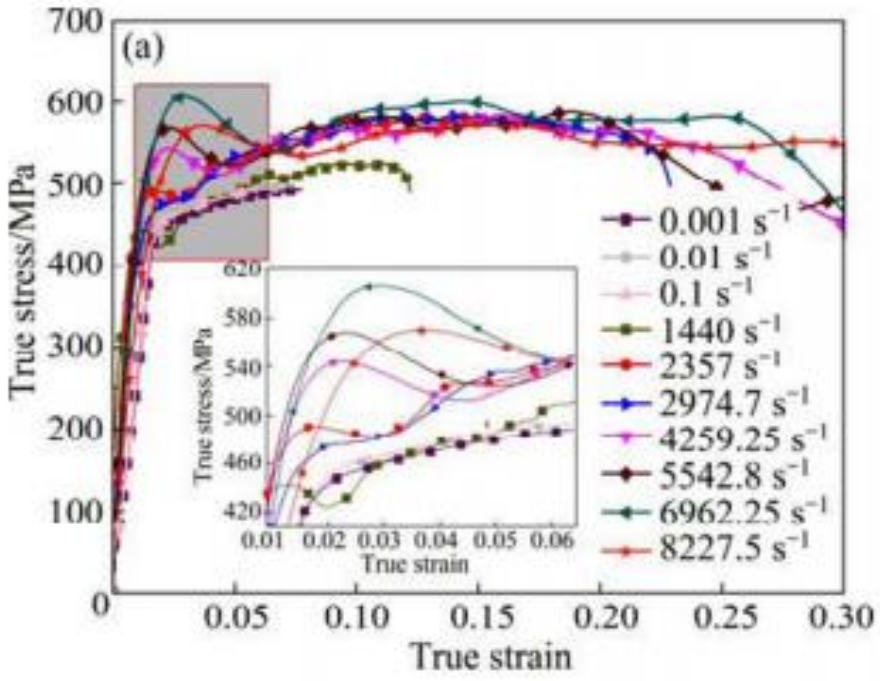

Figure 9: *True stress-strain curves of 2519A aluminum alloy at different strain rates under compression [23]*

Also, the mechanical behavior of mild steel tested in compression at the quasi-static test of 0.001 s^{-1} and high strain rate tests at around 1000 s^{-1} has been investigated by Singh et al. [24]. It can be clearly seen from Figure 10 that the compressive behavior of mild steel at a high strain rate is different than that at the quasi-static conditions. Evidently, the materials are strain-rate sensitive in compression.

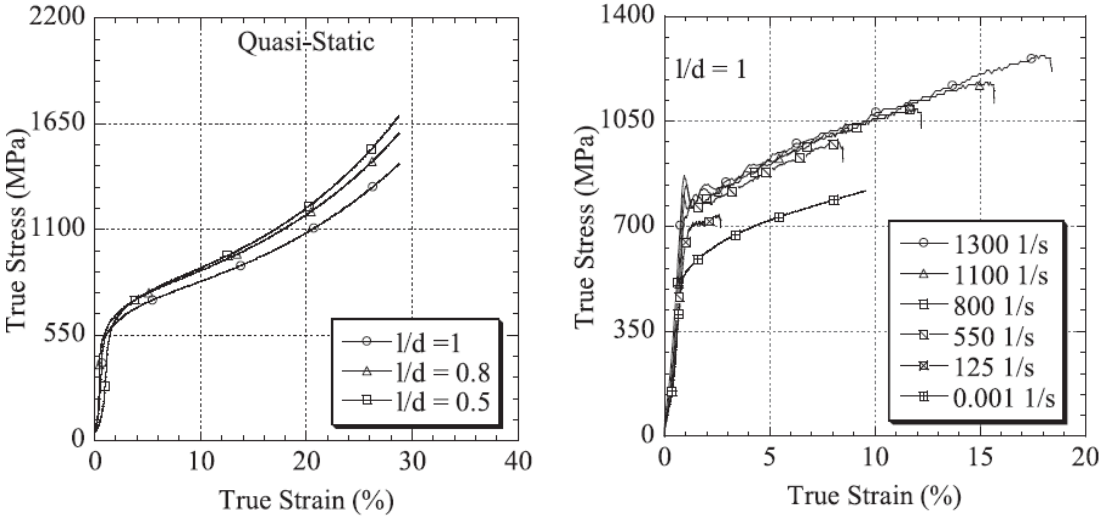

Figure 10: *Comparison of true stress-strain curves at quasi-static and high strain rates of a mild steel [24]*

Detailed study of dynamic (from 0.1 to 500 s^{-1}) tensile behavior of bainitic and quenched-tempered (QT) martensitic steels has been done by Zhou et al. [25]. They tested 3 different heat-treated samples. The first sample referred as B1 was austenitized at 880 ºC, kept isothermally at 300 ºC for only 40 minutes followed by the air cooling, B3 sample was austenitized at the same temperature but kept isothermally at 250 ºC for 48 hours which eventually was left for cooling at the room temperature whereas QT samples were quenched immediately in water. The quasi-static and dynamic tests results are shown in Figure 11.

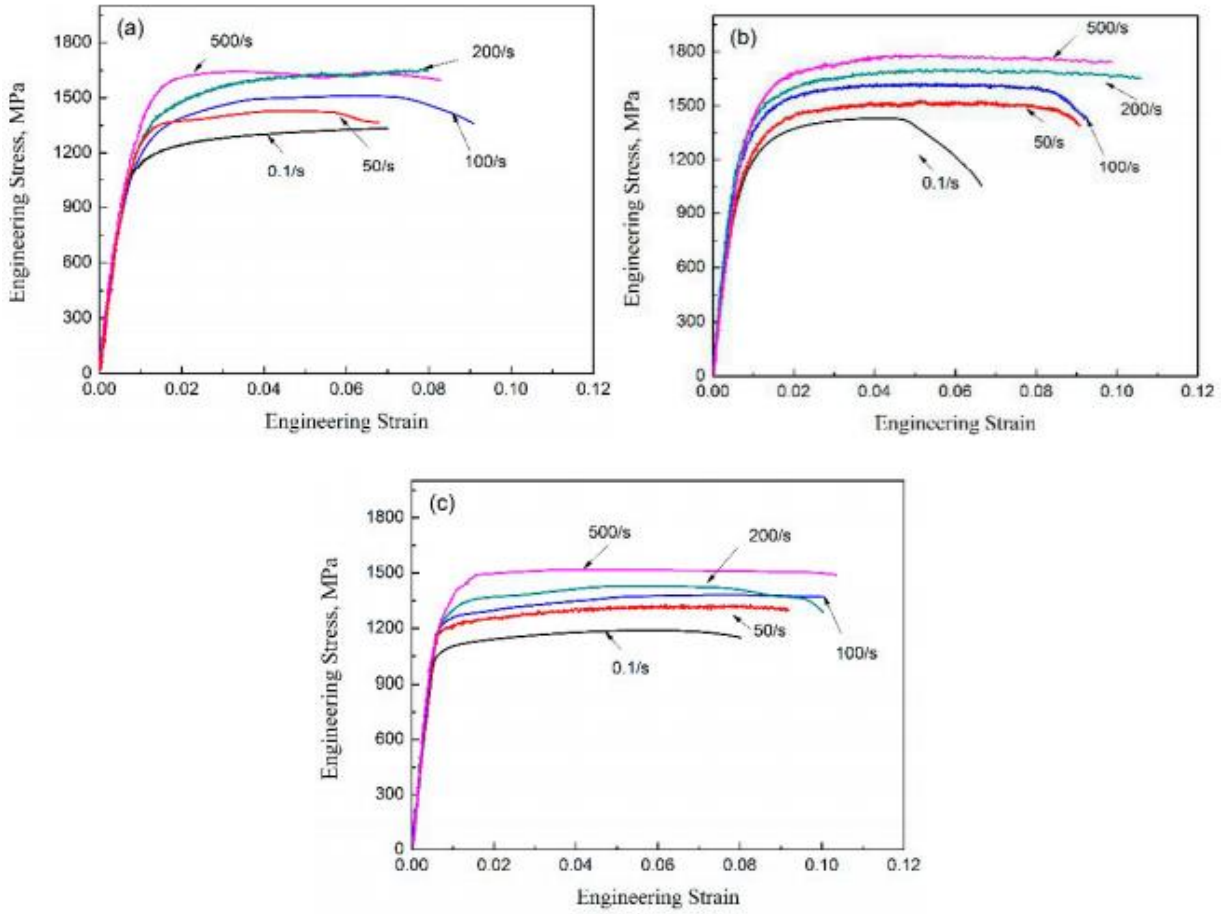

Figure 11: *Engineering stress-strain curves of(a) B1, (b)B3 and (c)Q&T samples [25]*

The experimental results showed that the ultimate tensile strength and elongation of all the tested samples increased with an increment of strain rates. When the strain rate is increased from 0.1 to 500 s^{-1}, the Q&T sample was most sensitive to the tensile strain rate among the three samples. The ultimate tensile strength of the Q&T sample gradually increased by about 34% (from 1127 MPa to 1516 MPa) whereas the tensile strength of B1 and B3 samples increased by 29 % and 23% respectively.

Sudden increases in shear stress were presented by Clifton [26] at high strain rates experiments of the order of 10^5 s^{-1} on 1100-0 aluminum as shown in Figure 12. At lower strain rates (below 10^5 s^{-1}), the shear stress, τ, of tested aluminum increased marginally with the strain rate, but on the other hand, sudden hardening was recognized as the strain rate of 10^5 s^{-1} was achieved in the experiment. This sparked the debate among the scientists making them believe that there might be limiting strain rate at which the strength of the material gets closer to infinity. [7]

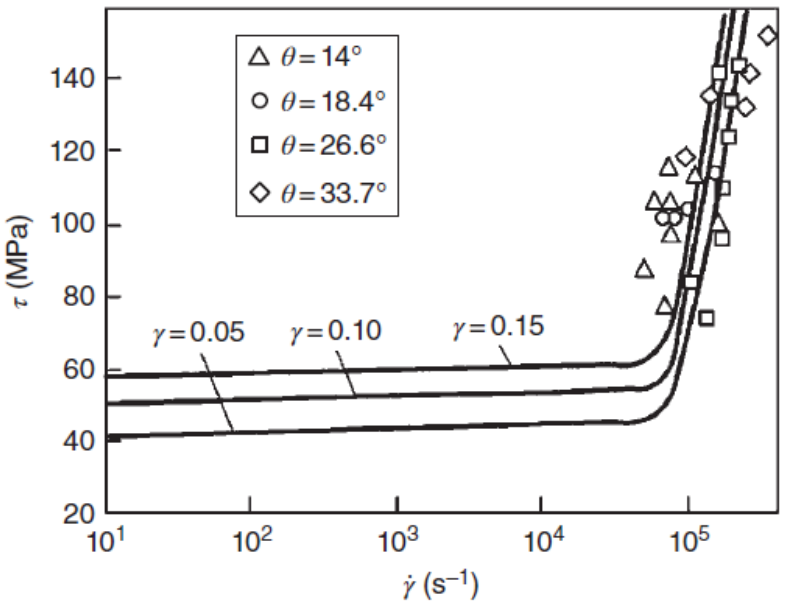

Figure 12: *Comparison of shear stress at different shear strain rates for 1100-0 aluminum [7]*

1.4 Correlation Between Applied Stress and Dislocation Velocity

The mechanism responsible for the plastic deformation of metals at the micro-scale is discussed briefly in this section. Also, the mechanism controlling the deformation at different strain rates and the main dislocation motion responsible for plastic deformation in the aluminum alloy is discussed briefly.

1.4.1 Dislocation Dynamics

There are many theories to interpret the plastic behavior of all materials like dislocation glide, mechanical twinning, phase transformations, etc. But in this section, only dislocation motion responsible for plastic deformation will be discussed briefly. Dislocations are linear crystal defects within a crystal structure that strongly influence many properties of

materials. Shear strain is produced by the movement of dislocations and their movement is influenced by shear stresses. [7,8]

Edge, screw, and mixed dislocations are the three types of dislocations. Figure 13 illustrates an edge dislocation moving under the influence of shear stress (τ). The force on the dislocation per unit length is then given by

$$F = \tau b \tag{1.24}$$

where b is the dislocation Burgers vector which describes the magnitude and direction of lattice distortion resulting from a dislocation in a crystal lattice.

In the case of an edge dislocation, Burger's vector is on the glide plane and perpendicular to the dislocation line. In this type of dislocation, the dislocation line moves in the direction of the Burger's vector. But on the other hand, Burger's vector and dislocation line are parallel and the dislocation line moves perpendicular to the Burger's vector in the case of a screw dislocation. In practice, mixed dislocation is the most common dislocation. As shown in Figure 13(a), the movement of dislocations is hindered by frictional forces and stresses should be applied for its motion. If the dislocation covers the distance of the Burger vector, it will reach a new equilibrium position. Similar movements of arrays of dislocations within a crystal lattice will produce a shear strain (γ =tan θ), as shown in Figure 13(b).

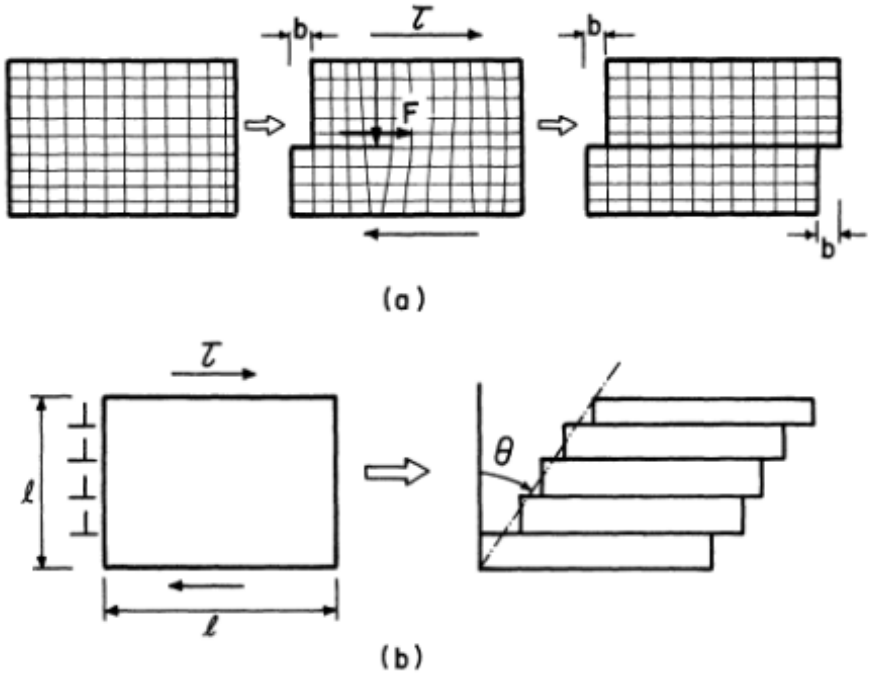

Figure 13: *(a) Movement of one dislocation causing displacement b; (b)progression of the array of dislocations causing shear strain [7]*

As mentioned before, the mechanical behavior of different materials at high strain rates has been studied extensively over the years. At very high strain rates or dislocation velocities, three regions of materials response are defined (Regions I, II, III) as shown in Figures 14 and 15 [7,27]. These three regions define three different mechanisms governing plastic deformation. Thermally activated dislocation motion is the main governing mechanism in the region I while phonon drag, and relativistic effects are other mechanisms in regions II and III respectively.

Regazzoni et al. [28] reported that during high strain rate deformation of metals, the strain rate sensitivity increases at strain rates above $10^3\,s^{-1}$. Follansbee et al. [29] also demonstrated that the stress increases gradually with the logarithm of strain rate at low strain rates from the results obtained in pure polycrystalline copper. In this regime, the strain rate sensitivity ($1/m = \partial \ln\sigma / \partial \ln\dot{\varepsilon}^{o}$) is typically on the order of 0.001. Above $10^3\,s^{-1}$, 1/m increases and reaches the value 0.2 for a strain rate of $2*10^4\,s^{-1}$. This similar behavior has been observed in materials such as in aluminum single crystals, in polycrystalline aluminum, in zinc crystals, in polycrystalline copper, in mild steel and in high strength steel [28].

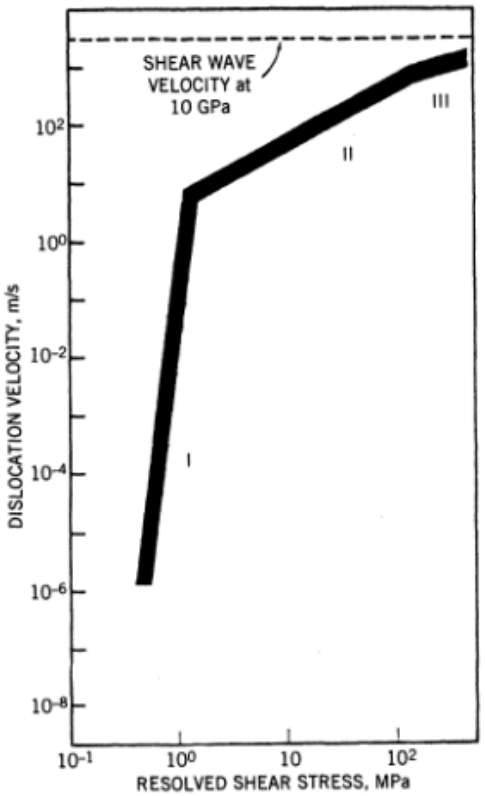

Figure 14: *Schematic representation of the stress-velocity behavior of nickel. Three regions of response can be established: region I, II and III [7]*

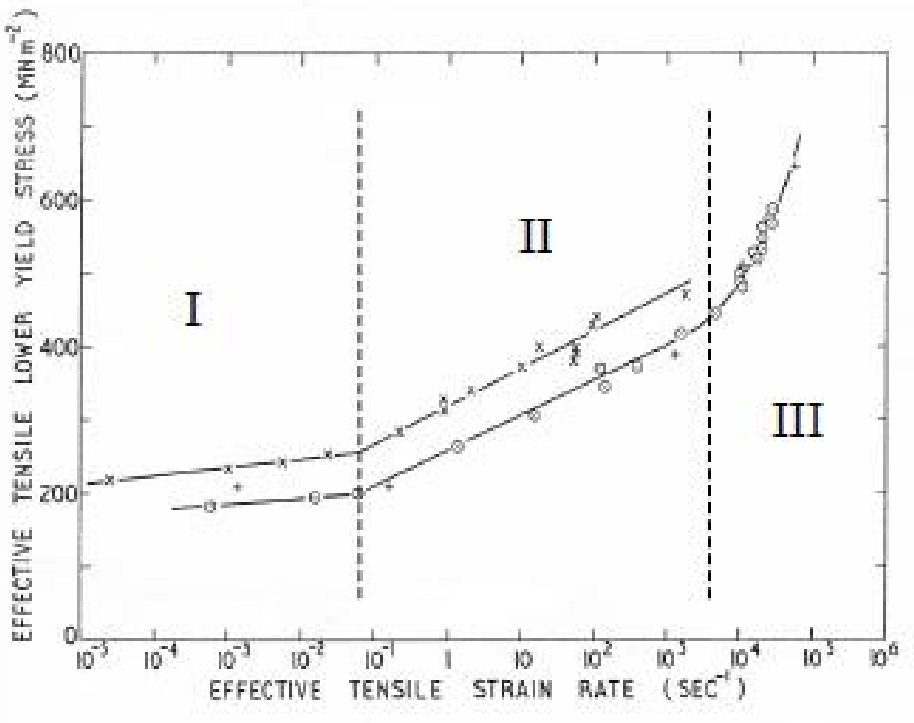

Figure 15: *Effective tensile yield stress versus strain rate of En3B steel comparing the results of tension(x) and punch (+) tests illustrating 3 response regions of strain rate sensitive behavior [27]*

The increase in strain rate sensitivity at high strain rates has been understood as a change in the mechanism controlling the plastic deformation. It has been interpreted that dislocation motion is governed by thermal activation in the low strain-rate region. After the strain rate is increased, thermal activation plays less role in moving a dislocation. The dislocation motion is steady at high strain rates and the mechanism changes to dissipative drag mechanisms. [28, 30-32] However, Weertman [32] approximated based on dislocation velocities that this transition occurs at high strain rates of 10^4 s^{-1}. Also, Follansbee [33] presented that the transition from thermally activated dislocation motion to phonon drag takes place at high rates of 10^4 s^{-1} for copper, copper-aluminum and stainless steels. Figure 15 shows that the transition from the region I to region II takes place at a strain rate of 0.1 s^{-1}, which is in contradiction to other results. Most often, it has been concluded that this transition occurs typically at 10^3 s^{-1} [28,29].

In the following subsection, thermally activated dislocation motion will be explained briefly. The reader is advised to other articles for detailed information on the other two mechanisms at very high strain rates [28-33].

1.4.2 Thermally Activated Dislocation Motion

The movement of dislocations in a lattice is continuously hindered by obstacles such as vacancies, inclusions, small-angle grain boundaries precipitates and so on. These obstacles are primarily responsible for plastic deformation. Moreover, obstacles themselves can oppose their own movement. [7, 34] It is also acknowledged that plastic deformation of metals occurs due to creep. The general misconception about the phenomenon of creep is that it occurs only at high temperatures. It may occur from about -273 ^{0}C to the melting point of metals. Fluctuations of yield stress at different temperatures and strain rates are other indications of dynamic plastic deformation. These events of deformation were first reported by Becker in 1925 and indicated that plastic flow in metals takes place when the obstacles are overcome by thermal fluctuations. [35] So, for the thermally activated dislocation motion Arrhenius equation can be written as:

$$\dot{\varepsilon} = \dot{\varepsilon_0}\, exp - [\frac{H(\sigma)}{kT}] \tag{1.25}$$

where $\dot{\varepsilon}$ is average strain rate; $\dot{\varepsilon_0}$ includes many factors such as attempt frequency and thermally activated strain increment, H(σ) is an activation enthalpy(energy) to prevail the obstacle, k is the Boltzmann constant and T is absolute temperature.

Schematic representations of the ways to overcome the obstacles are given in Figure 16. Peierls-Nabarro forces generally oppose the movement at an atomic level. In order to move from one equilibrium position to the next, a dislocation has to overcome an energy barrier called Peierls-Nabarro energy. The stress required to overcome a dislocation without any external help is Peierls-Nabarro stress. Besides this stress, a dislocation may face other obstacles which are divided into two types:

- obstacles with bigger stress regions (10 atomic diameters or greater)
- obstacles with shorter stress regions (less than 10 atomic diameters)

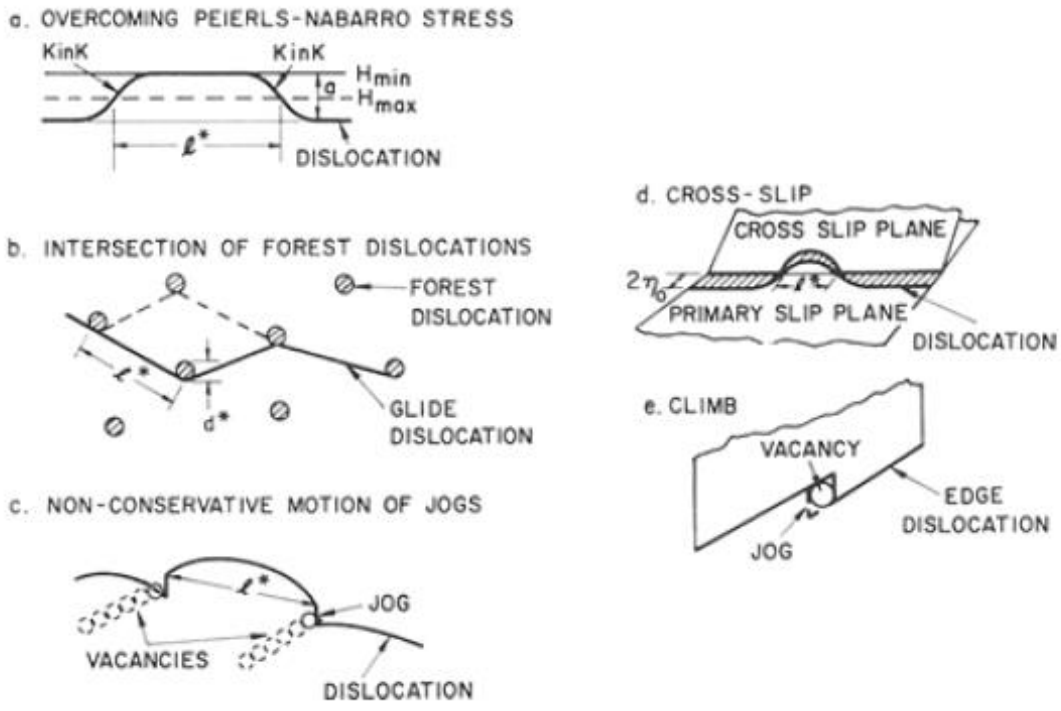

Figure 16:*Thermally activated dislocation mechanisms [35]*

A significant amount of energy is required to overcome the obstacles with large stress fields. Therefore, they are called athermal obstacles and thermal activation is unable to overcome this type of obstacle. Parallel slip plane dislocations and secondary particles are the most common types of athermal obstacles. [35]

But on the other hand, thermal activation can contribute to overcoming obstacles of shorter stress fields (also known as thermal obstacles). Some common examples of thermal obstacles are Peierls-Nabarro stress, jog formation in the intersection of forest dislocations, the non-conservative motion of jogs, and cross-slip in screw dislocations and climb of edge dislocations. Moreover, the dislocations can also encounter short-stress obstacles superposed on big stress field obstacles. [35]

The Peierls-Nabarro stress is a short-range barrier and important for body-centered cubic (BCC) metals like Iron. But for face-centered cubic (FCC) metals like aluminum, dislocation forests are the primary short-range barriers at lower temperatures. The dislocations that stand up and through which the moving dislocation must move are called forest dislocations. Shown in Figure 17 is a dislocation moving through a dislocation forest intersecting the slip plane. [7] Dislocation intersections cause jogs formation which generally reduces dislocation mobility but increases dislocation length. These jogs usually do not move easily resulting in material strain hardening.

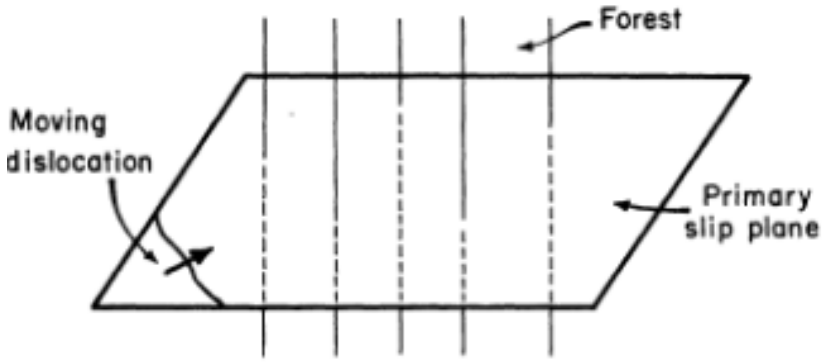

Figure 17: *Moving dislocation cutting through a dislocation forest [7]*

1.5 High Strain Rate Behavior of Aluminum alloys

Many researchers have found out that the aluminum and aluminum alloys exhibit low strain rate sensitivity, but these materials are also sensitive to strain rates at strain rates higher than 10^3 s^{-1} at normal room temperature. Tanaka et al. [36] carried out high strain rate compression tests on pure aluminum, aluminum-copper alloy, and duralumin. Basically, it was concluded that in the case of pure aluminum, the flow stress showed a dependency on strain rates between 10^{-4} s^{-1} and 10^3 s^{-1} as shown in Figure 18. The strain rate sensitivity although increased above strain rates of 10^3 s^{-1}. Contradictory, the other two aluminum alloys displayed zero strain rate sensitivity at room temperature. Hence, it can be concluded that with the increment of alloying elements on aluminum and heat treatment methods, the strain rate sensitivity tends to decrease [18, 36, 37]. But strain rate sensitivity of AlMgSi alloy and pure aluminum was also found to be temperature-dependent in the range 430-670 K [6].

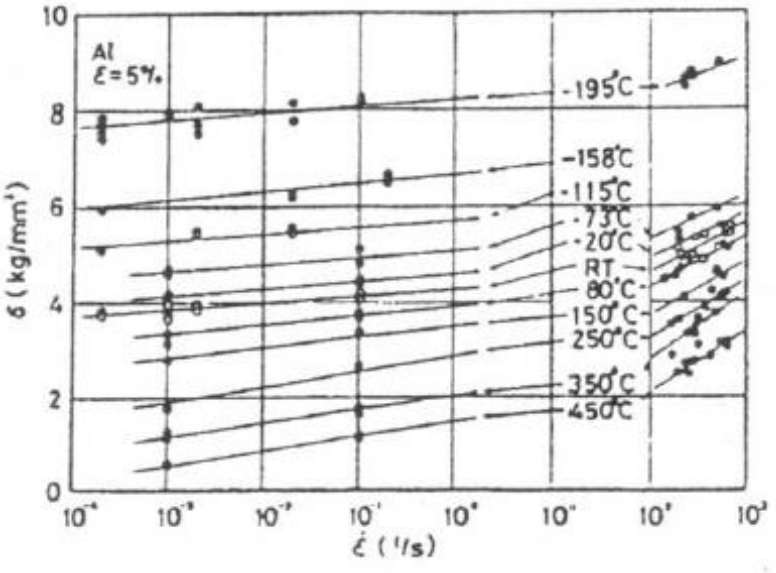

Figure 18: *Dependence of flow stress on strain rate for pure Aluminum [36]*

El-Magd et al. [38] carried out compression tests on the cylindrical specimens of AA 7075 at strain rates of 0.001 s^{-1} to 5000 s^{-1} and temperatures up to 200 ^{0}C. Experimentally determined flow curves are represented in Figure 19. The stress-strain curves of quasi-static tests increase regularly with the increase in strain due to strain hardening. Likewise, at strain rates greater than $10^3 s^{-1}$, there is an increase in flow curves and moreover, there is also a decrease in the value of stress after the maximum stress point. This usually happens due to adiabatic heating in high strain rates during the deformation process leading to an increase in temperature of the specimen. It can be clearly seen that the aluminum alloy 7075 exhibits little strain rate sensitivity at room temperature but at the higher temperatures, there is an increase in strain rate sensitivity as well as ductility.

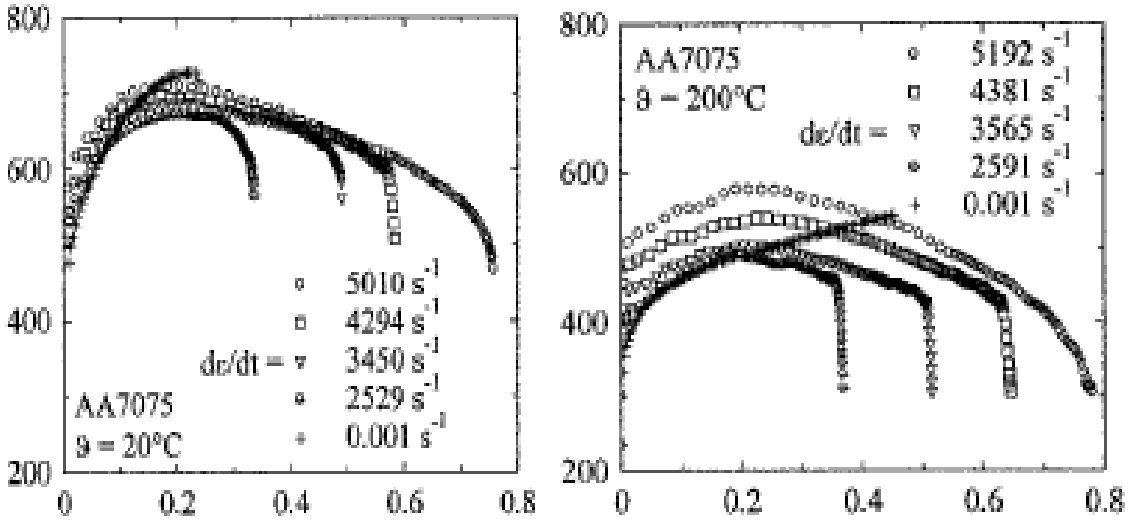

Figure 19: *Stress-strain curves of AA7075 at different strain rates and temperature; True stress (MPa) in the y-axis and true plastic strain in x-axis [38]*

Work done by Mishra et al. [39] on the high strain rate flow behavior of 7055 and 7017 aluminum alloys showed that the dynamic compressive stress-strain response of 7XXX series alloys can be divided into 3 regions as shown in Figure 20. In the region I, there is a quick work hardening up to the ultimate strength followed by a slow decrease in strength. Slow decrease with an insignificant drop in strength can be seen in region II followed by a rapid decrease in region III. The decrease in the strength at high strain rates is caused by the formation of adiabatic shear bands (ASB) and cracking induced by ASB. Likewise, there is no drop of strength in quasi-static compressive regions which suggests that the governing mechanisms in the two conditions are different [39].

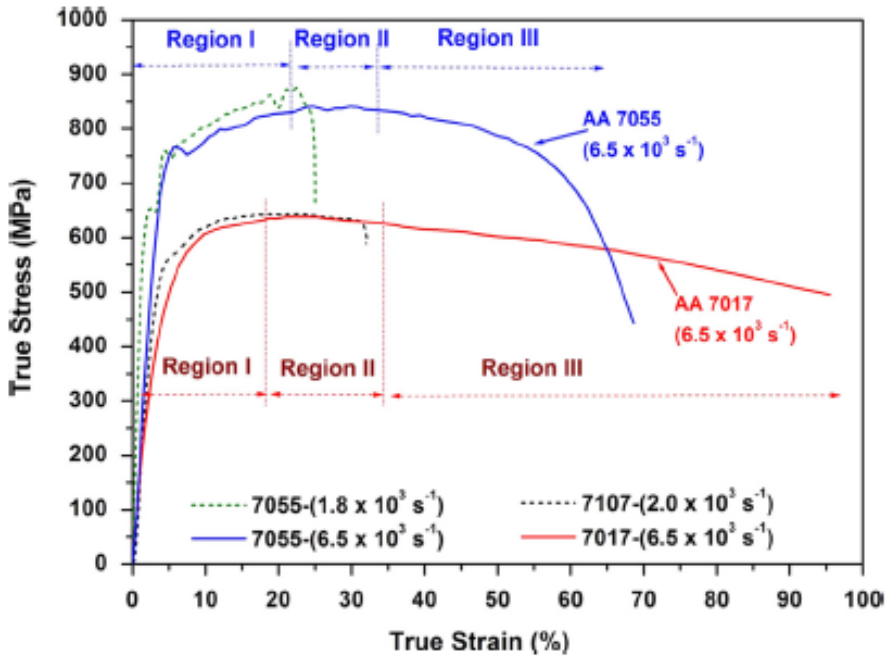

Figure 20: *Dynamic flow curves at high strain rates [39]*

The strain sensitivity parameter of conventional aluminum and its alloys was measured by Lindholm et al. [40] with respect to static flow stress evaluated at a strain rate of $1s^{-1}$. It can be clearly seen in Figure 21 that pure aluminum is more sensitive to strain rate and the sensitivity parameter decreases along with an increase in alloying contents and heat treatment methods.

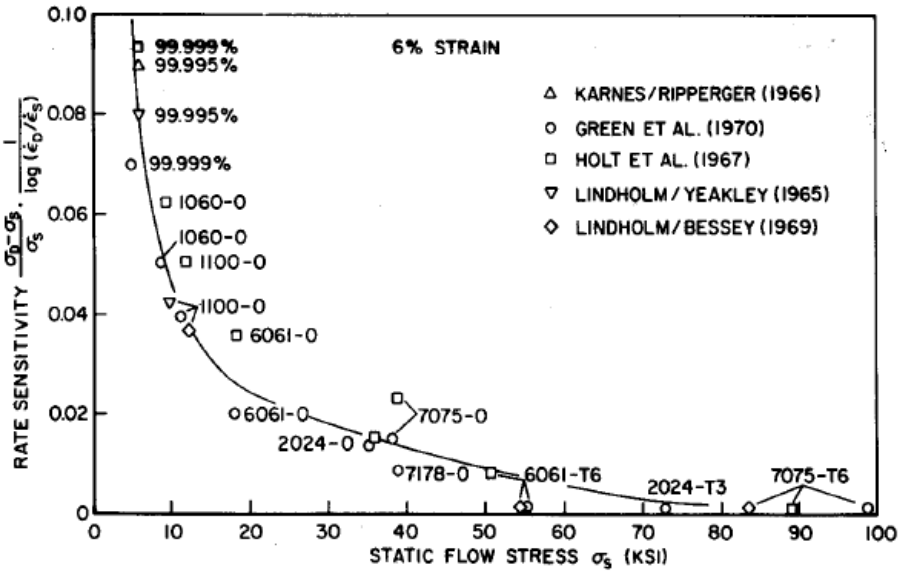

Figure 21: *Strain-rate sensitivity of aluminum and aluminum alloys as a function of yield strength [40]*

The comparison of strain rate sensitivity of conventional (CG) aluminum (Al 99.5) and ultrafine-grained (UFG) aluminum has been done by May et al. [41]. The UFG aluminum was produced by accumulative roll bonding plastic deformation technique. Figure 22 shows the comparison of the strain rate sensitivity measured in different temperatures. It can be clearly seen that UFG aluminum is more sensitive to strain rates than CG aluminum and it increases gradually with the increase in temperatures. At a temperature of 250 ºC, the value of m= 0.25 is reported for UFG aluminum.

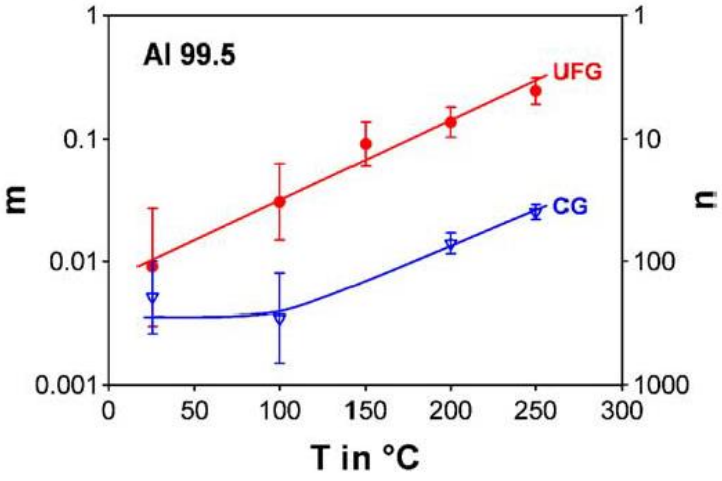

Figure 22: *Strain rate sensitivity(m) versus temperature for conventional Al and ultrafine-grained Al [41]*

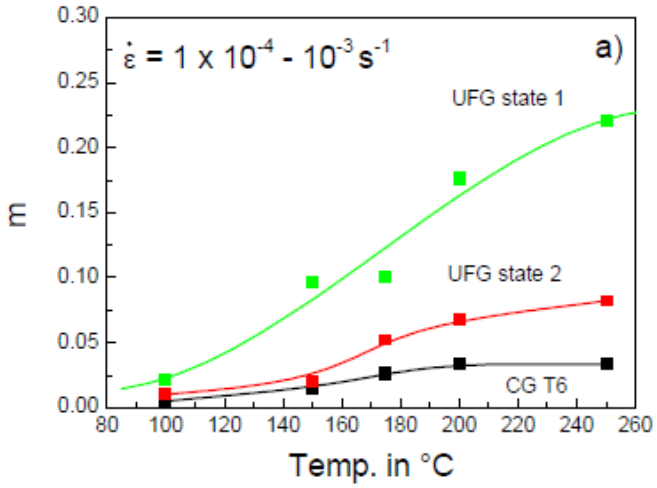

Figure 23: *Comparison of strain rate sensitivity of conventional and ultrafine-grained AA 6061 [42]*

Also, the strain rate sensitivity of AA6061 has been studied by Priftaj et al. [42] using CG aluminum alloy and ultrafine-grained alloys processed by two different methods. The first UFG alloy (state 1) was heat-treated at 530 ºC for 1 hour followed by quenching in water and processed by equal channel angular pressing (ECAP) for 6 passes at 100 ºC

whereas second UFG alloy (state 2) was heat treated and quenched as the first one, further annealed for 18 hours but processed by ECAP for only 2 passes. The strain rate sensitivity of the alloys measured at the strain rate from 10^{-4} s^{-1} to 10^{-3} s^{-1} is shown in Figure 23. The difference in measured strength of two UFG states is only about 5 % but the variation between two UFG alloys is observed in microstructure where the degree of orientation of grains changes from low angle boundaries to high angle boundaries with the increase in the number of ECAP passes. So, it is obvious that strain rate sensitivity is enhanced by the UFG microstructure and increases with temperature. Moreover, the sensitivity parameter increases for state 1 with high angle grain boundaries as the materials become softer and it also increases sharply with an increase in temperature.

1.6 Material Modelling with Johnson-Cook (JC) Constitutive Model

The accuracy of the finite element numerical simulation depends notably on the accuracy of the deformation behavior represented by the constitutive equations. So far, much research has been done to develop the constitutive equations of materials from the experimental results to describe the relationship between flow stress and deformation behavior under different loading conditions. These constitutive equations can be divided mainly into two categories: empirical constitutive models and physical-based models.

Empirical models, e.g. Johnson-Cook (JC) model [43], Klopp model [44], Khan–Liu (KL) model [45], etc. predict the flow behaviors of metallic materials during high strain rate loading conditions. These models predict the mechanical properties of materials with limited number of constants which can be easily derived from the experiments. Among these models, the JC model is widely used and also embedded in many FE software to simulate the flow behavior of a variety of materials loaded under dynamic conditions.

The physically-based models such as Zerilli-Armstrong (ZA) model [46,47], Mechanical threshold stress (MTS) model [48], Bonder-Partom (BP) model [49], etc. elucidate the physical mechanism of material behavior based on the thermal activation and dislocation dynamics. The main disadvantage is that a large number of experimental data are needed for these types of physical-based models.

The JC constitutive model was first proposed in 1983 [43]. It can be expressed as follows:

$$\sigma = (\mathrm{A} + \mathrm{B}\varepsilon^{\mathrm{n}})(1 + \mathrm{C}\ln\dot{\varepsilon}^{*})(1 - \mathrm{T}^{*\mathrm{m}}) \tag{1.26}$$

$$T^{*} = \frac{T - T_{ref}}{T_{melt} - T_{ref}} \tag{1.27}$$

where σ is the equivalent stress, ε is the equivalent plastic strain, $\dot{\varepsilon}^* = \dot{\varepsilon}/\dot{\varepsilon}_0$ is dimensionless strain rate with $\dot{\varepsilon}$ being the equivalent strain rate, $\dot{\varepsilon}_0$ is the reference strain rate. T_{ref} and T_{melt} are the reference and melting temperature respectively.

The five unknown material constants are A, B, n, C and m, which can be calculated by fitting the model to the experimental stress-strain curves under different strain rates and temperatures. The expressions in the first set of brackets describe the strain hardening. Moreover, the constants in the second and third sets of brackets represent hardening caused by the strain rate and thermal softening of the material respectively. In the fitting process, the constants in the first bracket are determined first. A is the yield strength at reference strain rate and temperature, the constant B corresponds to the amount of the strain hardening of the materials at the strain of one and n is the strain hardening coefficient of the materials.

Johnson and Cook presented a constitutive model from the torsion tests over a wide range of strain rates from quasi-static to about 400 s^{-1} for three materials; OFHC copper, Armco iron and 4340 steel. The Armco iron and 4340 steel showed very good agreement but OFHC copper results did not agree very well.

Over the years, hundreds of modifications have been done to the original JC model but only a few are discussed here. Eq. (1.26) can produce enough accurate results but for many ductile metals, the yield strength increases more rapidly with the strain rate than that described by the equation for higher strain rates than 10^3 s^{-1}. So, Rule and Jones in 1997 [50] revised and modified the JC strength model to increase the strain rate sensitivity minimizing changes to the original model. The modified model has the following form:

$$\sigma = (C_1 + C_2\varepsilon^N)[1 + C_3 ln\varepsilon * + C_4(\frac{1}{C_5 - ln\varepsilon *} - \frac{1}{C_5})](1 - T^{*M}) \qquad (1.28)$$

where $C_1\ to\ C_5$, N and M are empirical coefficients and exponents. The second expression is termed as a strain rate sensitivity factor. The term 1/ ($C_5 - ln\varepsilon$*) tends to infinity as the strain rate reaches the critical strain rate. At strain rates lower than unity, the strain rate sensitivity factor$C_4(\frac{1}{C_5 - ln\varepsilon *} - \frac{1}{C_5})$ is removed. They evaluated the revised model for 7075-T6 aluminum, OFHC copper, wrought copper, wrought iron and high-strength steel and it appeared capable of representing the mechanical behavior of tested metals at a wide range of strain rates.

Chen et al. [51] realized that the original JC model could not illustrate the modification of the work hardening of AA 7050 from positive to negative values. Hence, they also

modified the original JC model by studying the mechanical behavior of aluminum 7050-T7452 alloy performing the quasi-static and dynamic uniaxial compression tests over a wide range of strain rates and temperatures and determining the work hardening rate (Q_{JC}) as:

$$Q_{JC} = Bn\varepsilon^{(n-1)}(1+C\ \ln\dot{\varepsilon}*)(1-T^{*m}) \quad (1.29)$$

Also, Tan et al. [52] modified the JC model by integrating variable strain rate hardening coefficients with strain and strain rate. They used a binary quadratic polynomial regression model and found out that the proposed model had higher accuracy than the existing model to predict the tensile flow behaviors for 7050-T7451 aluminum alloy at high strain rates. Further reading can be done in reference [52]. It is clear that the JC model is a very flexible and reasonably accurate model that can be modified according to the change in applications of various materials as done by many researchers.

1.7 Effect of Friction and Specimen Size in Compression tests at High Strain Rates

When the coefficient of friction is zero at the interface between the specimen and the pressure bars in the compression tests, the deformation of the specimen is uniform as shown in Figure 24a. Contrarily, when the frictional force exists at the contact interface, the movement of two sides of the cylindrical specimen are restricted during the compression tests. As a result, the cross-sectional area of the specimen varies generating barrel-like shape as represented in Figure 24b. [53] The friction at the interfaces will result in non-uniform stress distribution and the properties obtained from these types of tests can be unreliable.

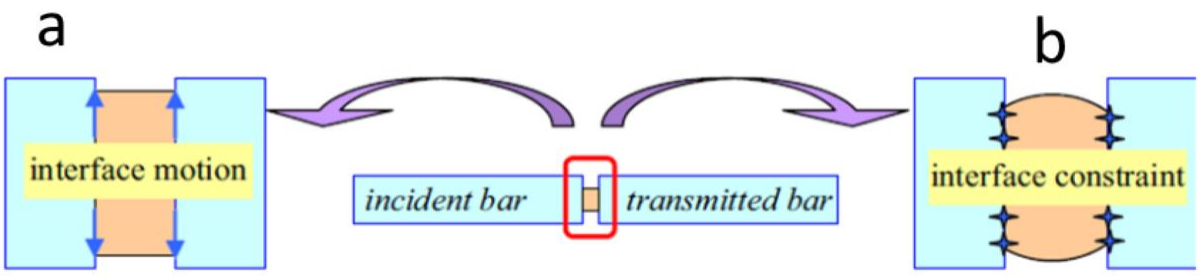

Figure 24: *Specimen deformation in compression at different interface conditions; (a) with lubrication and (b) friction [53]*

Improved estimation of the effects of the friction, inertia and specimen size in high strain rate compression test allows more precise determination of material behavior and its constitutive equations at high strain rates. The coefficient of friction (μ) in a compression test can be estimated roughly by Siebel's equation [54]:

$$P = (1 + \frac{\mu\, D}{3L})\sigma_{\varepsilon} \tag{1.30}$$

where P is applied pressure, D and L are diameter and length of specimen respectively and σ_{ε} is material flow stress. Davies et al. [55] found the friction coefficient of 0.02-0.06 in a compression test using a constant specimen length to diameter ratio of 0.5.

The effects of the specimen size and friction in the high strain rate compression tests have been studied by Gorham [56] using copper. He suggested that specimen size can influence the friction since larger specimens deformed at the same rate involve larger radial displacements than small specimens. Lubricant breakdown is more likely when using larger specimens which may lead to larger interfacial friction. Also, he suggested employing specimens of an aspect ratio L/D= 0.86 to avoid inertia effects.

Nobuhiko et al. [57] recommended utilizing hollow specimens instead of the cylindrical specimen to reduce the friction effects in the compression test that will allow to decrease contact area between the specimen and pressure bars. But they observed a reduction in stress level which occurred due to buckling and finally concluded that thin hollow specimens may be inappropriate for these impact tests. Wang et al. [58] reported that friction has a significant effect on the yield behavior as well as on the post-yield behavior of the materials. They [58] reduced the friction effect on the yield behavior using petroleum jelly.

The effect of the specimen size on the flow stress of aluminum 7075-T6 was studied by Meyer et al. [59] who found that the contribution of interface friction may depend on the specimen size. The effect of specimen length to diameter ratio in dynamic compression tests was investigated in detail by Yokoyama et. al [60] using Al 6061-T6 at strain rates higher than 1000 s^{-1}. They recommended that the most favorable specimen geometry is with a L/D ratio between 0.50 and 0.75 when the diameter ratio between the specimen and the used pressure bar is 0.5. However, different kinds of recommendations were provided by Irama et al. [61], who claim that the accurate mechanical properties can be obtained using specimen length to diameter ratio between 0.5 and 1 only if the specimen to pressure bar diameter is equal or less than 0.5. Also, an aspect ratio of 1 was suggested for moderate-high strain rates and moreover, inertia effects could be reduced using an aspect ratio of 0.5 for very high strain rates [62].

Liquid lubricants were found to be more effective in reducing the friction effect by Hall et al. [5] where they used different types of lubricants in the SHPB compression test of aluminum alloy. As a continuation of the work by Hall et al. [5], the appropriate specimen size, aspect ratio and effect of friction will be discussed in detail in the following sections.

1.8 Present Work

The main aim of the present work is to find the appropriate specimen dimension and length to diameter (L/D) ratio that can be used to characterize the high strain rate behavior of aluminum alloy 7050-T351. The role of the friction was also studied in these experiments by carrying out the experiments initially without any lubricant and later the same experiments with lubricant applied to the incident and transmitted bars. To provide this information, compression tests were performed at elevated strain rates and room temperature. Also, comparisons of the experimental results obtained using cylindrical and cuboid specimens were done. Then, the obtained experimental results were fitted to the Johnson-Cook constitutive model. The Johnson-Cook parameters derived were then used in the numerical simulations performed using LS-Dyna [63], a dynamic finite element code.

The experimental setup, specimen types, and geometry used in the compression tests are presented. Experimental procedures and numerical simulations performed are also discussed in detail. Moreover, the results from both experiments and simulations are presented with an explanation.

2. EXPERIMENTAL METHODS

High strain rate experiments were conducted using cylindrical specimens with diameters of 5mm, 6mm, 8mm, 10mm, and 12mm. Length over diameter(L/D) ratios of 0.6, 1 and 1.4 were used in each case. Also, some experiments were carried using cuboid specimens to compare the accuracy of the results with those obtained from the cylindrical specimens. Moreover, in order to study the effect of friction, the experiments were conducted twice, with and without lubricants applied between the incident bar and transmitted bar. Then, Johnson-Cook model parameters were determined from the experimental results that were later used in the numerical modeling.

2.1 Material and Specimens

Aluminum-alloy 7050-T351 (Table 2) belongs to the 7XXX series (Al-Zn-Mg-Cu) aluminum alloys. It is a solution heat-treated, stretched a controlled amount for stress relief and naturally aged. This kind of alloy has an attractive combination of strength, corrosion resistance characteristics including stress-corrosion cracking resistance. Automotive and aerospace industries utilize this alloy due to its excellent physical and mechanical properties. [3,64] The aluminum alloy used in the experiments was provided by Cenaero company based in Belgium and its physical properties are given in Table 3.

Table 2: *The chemical composition of Al 7050-T351[3, 65]*

Al	Si	Fe	Cu	Mn	Mg	Cr	Zn	Ti	Zr
Bal.	0.12	0.15	2-2.6	0.10	1.9-2.6	0.04	5.7-6.7	0.06	0.08-0.15

Table 3: *Physical properties of aluminum alloy 7050-T351[3]*

Density (kg/m^3)	Modulus of elasticity (GPa)	Poisson's ratio	Specific heat capacity (J/kg K)	Melting point(K)
2830	70	0.33	860	893

From Figure 25, it can be observed that a typical microstructure of 7050 aluminum alloy at room temperature consists of highly elongated bandlike grains aligned in the rolling

direction. The grain structure, size, and precipitates distribution vary with heat treatment. [66]

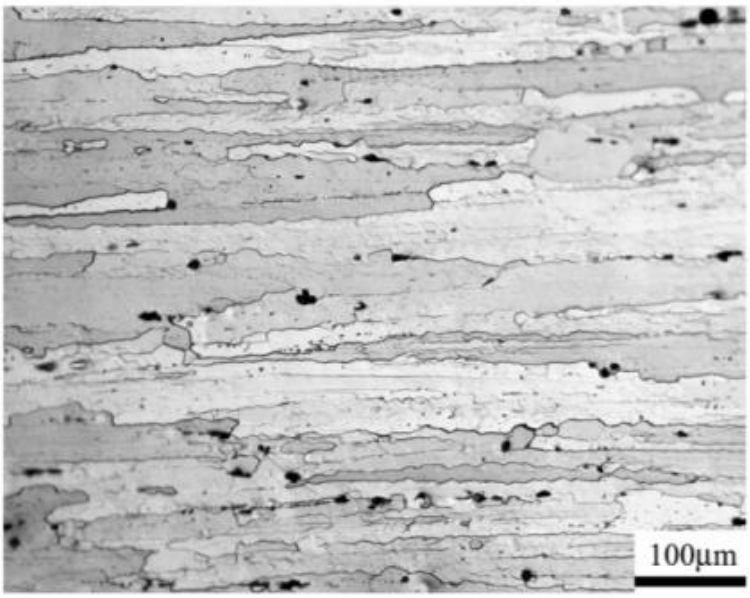

Figure 25:*Optical micrograph of 7050 aluminum alloy [66]*

The cylindrical and cuboid specimens used in the present work are shown in Figure 26. Compression specimens with varying dimensions were prepared to produce different kinds of aspect ratios: L/D =0.6, 1 and 1.4 respectively. The dimensions of all the specimens were measured prior to high strain rate testing.

(a)  (b) 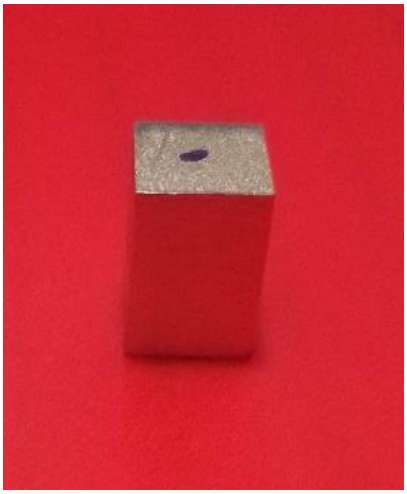

Figure 26: *(a) Cylindrical specimen and (b) cuboid specimen*

2.2 Equipment

2.2.1 Split-Hopkinson Pressure Bar Compression Apparatus

The dynamic compression experiments were carried out using the SHPB apparatus at the Technical University of Madrid. The schematic picture of the apparatus is shown in Figure 27, while the photographs are shown in Figure 28.

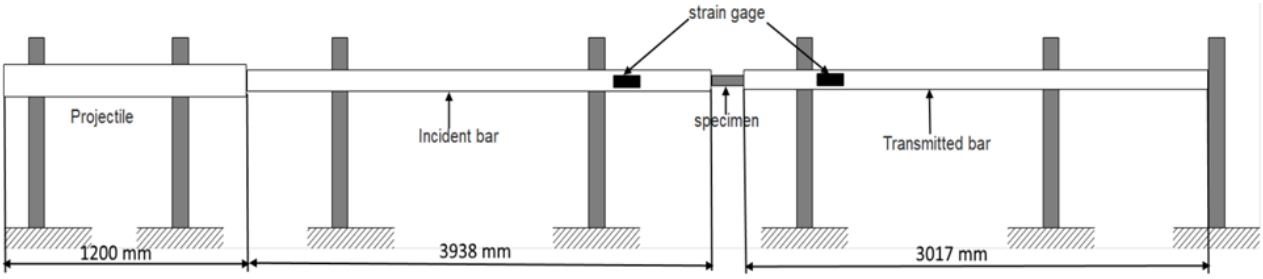

Figure 27: *Schematic of SHPB apparatus in Technical University of Madrid*

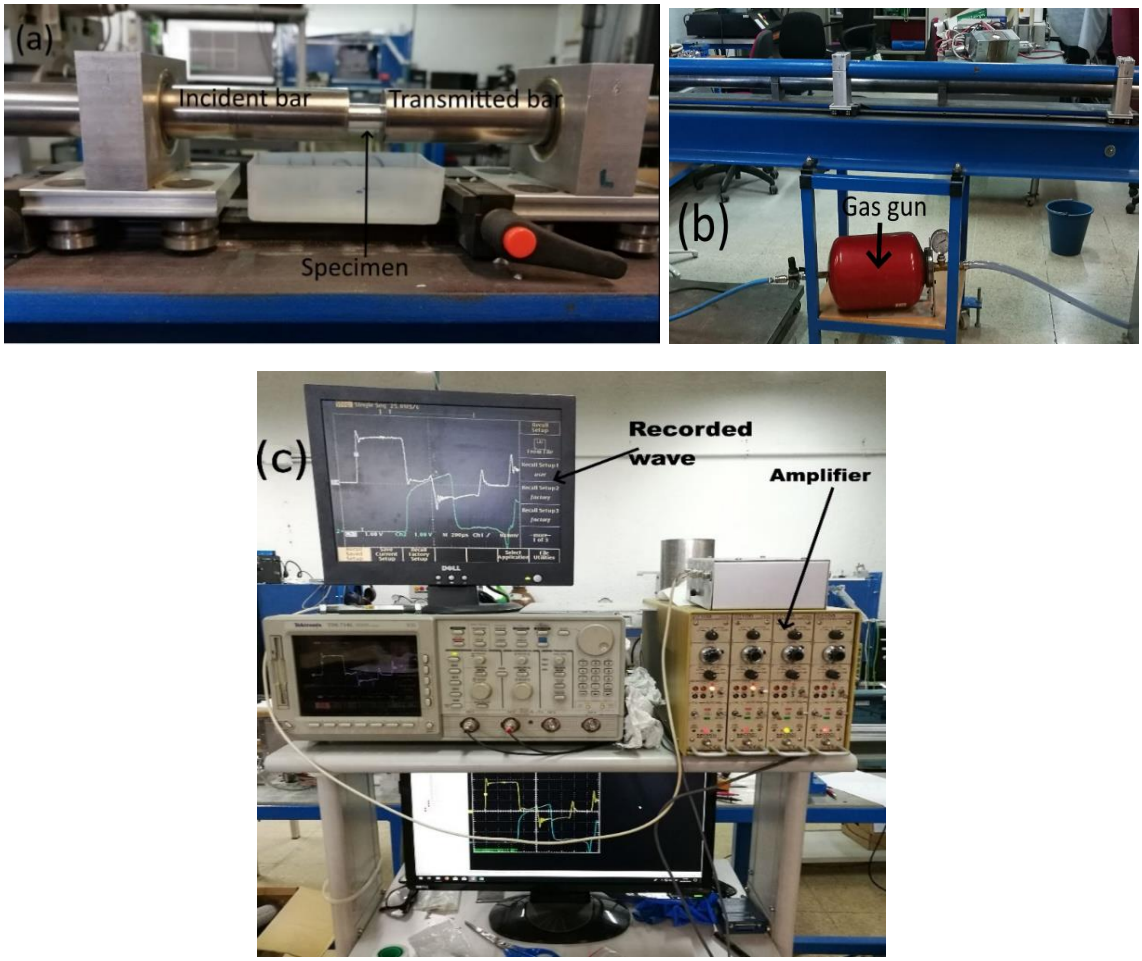

Figure 28: *Photographs of SHPB apparatus in Technical University of Madrid;(a) Specimen sandwiched between pressure bars, (b)Gas gun and (c) Output signal*

The SHPB test apparatus in the Technical University of Madrid has two long bars, one incident bar with a length of 3938 mm and a transmitted bar with a length of 3017 mm. The specimen for the high strain rate compression test is sandwiched between these two pressure bars as shown in Figure 28a. One of the requirements in high strain rate testing is that the incident pressure bar must be at least twice as long as the striker bar to avoid the interference of the recorded waves. So, the striker bar used was 1200 mm with the same cross-sectional area as the incident bar. The bars have a diameter of 25.4 mm and are made of maraging steel C250 and their elastic properties are listed in Table 4. The striker bar is located inside a hollow tube. The gas gun uses compressed nitrogen to propel the striker bar to impact the end of the incident bar. The time of passage and magnitude of the wave pulses are recorded by strain gages positioned at the mid-points of the incident and transmitted bars.

Table 4: *Elastic properties of the bars*

Density, ρ(kg/m^3)	7850
Young's modulus, E (GPa)	208
Poisson's ratio	0.3

2.2.2 Instrumentation

The incident and transmitted bars have four strain gages (2 gages each in transversal and longitudinal direction) in a full Wheatstone bridge as illustrated in Figure 29. The instrumentation used in the bars is Vishay micro measurement strain gages CEA-06-125UT-350 with nominal resistance 350 Ω, gage factor K =2.18 and excitation voltage of 7.5 V.

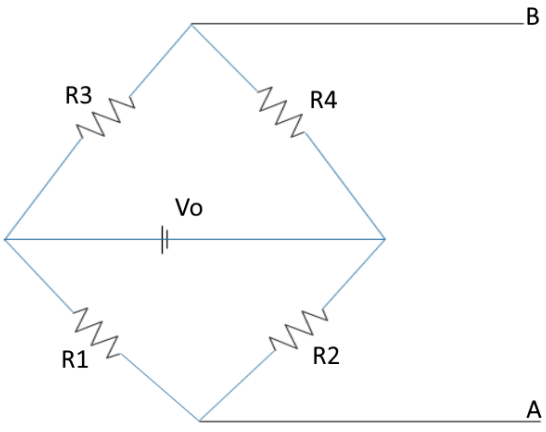

Figure 29: *Wheatstone bridge*

Gauge factor (K) is defined as the ratio of relative change in electrical resistance R_0 to the strain ε;

$$K.\varepsilon = \frac{\Delta R}{R_0} \tag{1.31}$$

Longitudinal (R_L)and transversal (R_T)resistance are then given by;

$$R_L = R_0(1 + K\,\varepsilon) \tag{1.32}$$

$$R_T = R_0(1 - \upsilon\,K\,\varepsilon) \tag{1.33}$$

where v is the Poisson's ratio. Then voltage in points A and B is;

$$V_{AB} = \frac{R_2R_3 - R_1R_4}{(R_1 + R_2)(R_3 + R_4)}V_0 = \frac{R_LR_L - R_TR_T}{(R_L + R_T)(R_L + R_T)}V_0 \tag{1.34}$$

Substituting the values of R_L and R_T from Eqs. (1.32) and (1.33) in Eq. (1.34), we get,

$$V_{AB} = \frac{R_0^2(1 + K\,\varepsilon)^2 - R_0^2(1 - \upsilon\,K\,\varepsilon)^2}{[R_0(1 + K\,\varepsilon) + R_0(1 - \upsilon\,K\,\varepsilon)]^2}V_0$$

$$V_{AB} = \frac{1 + \upsilon}{2}\,K\,\varepsilon\,V_0 \tag{1.35}$$

To increase the amplitude of signals obtained from the strain gages, the amplifier gain is used as presented in Figure 30.

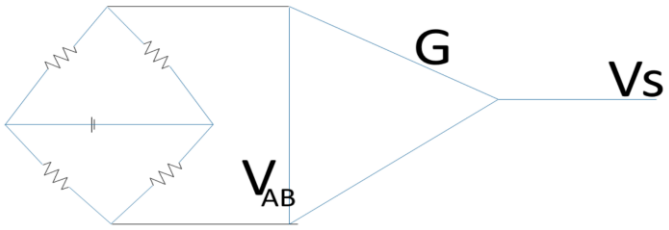

Figure 30: *Amplifier gain*

The output voltage (V_s) is:

$$V_s = \frac{1 + \upsilon}{2}\,K\,\varepsilon\,G\,V_0 \tag{1.36}$$

where G is the amplifier gain. And finally, the axial strain in the bars can be measured using:

$$\varepsilon = \frac{2}{1 + \upsilon}\,\frac{V_s}{K\,V_0G} \tag{1.37}$$

2.3 Experimental Procedure

The procedure of the experiment is quite simple. First, the transmitted bar is shifted back to its position, and the specimen is placed between the incident and transmitted bars. Then the amplifier gain in the input and output bars is adjusted according to the diameter of the specimen. The pulse shaper is also placed on the incident bar to obtain the smooth wave signals. After that, the incident bar is impacted by the striker bar with the preset velocity. The dynamic compression tests were carried out with a striker velocity of 8 m/s. A compressive incident stress-wave is produced once the striker bar hits the free end of the incident bar. Once this wave reaches the bar-specimen surface, a part of the pulse is reflected while the remainder of the pulse is transmitted through the specimen. These waves are recorded by the strain gages. The strain-gage data measured as a function of time in the experiment is shown in Figure 31.

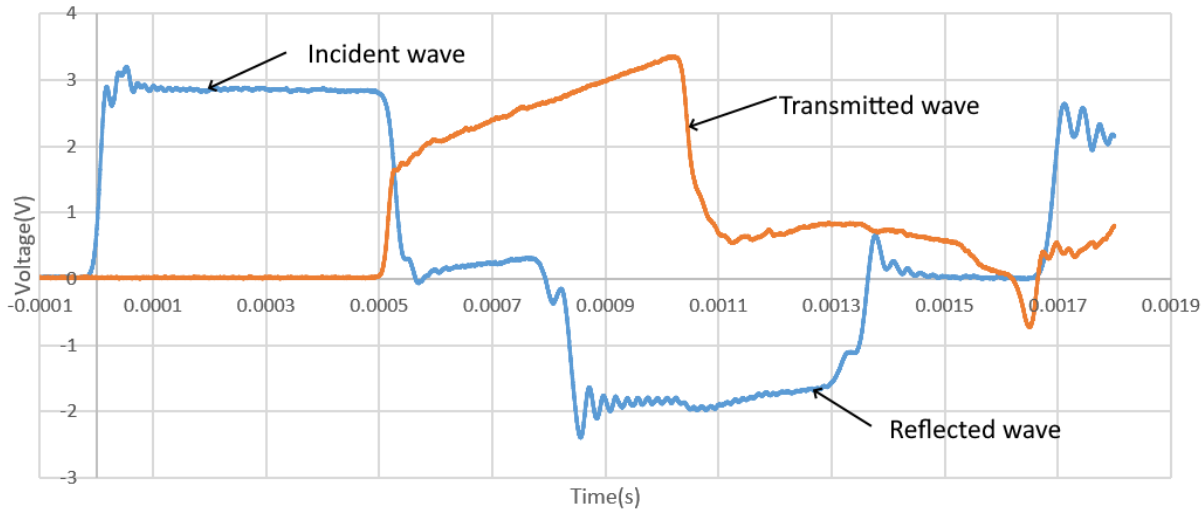

Figure 31: *Waves recorded in the experiment*

The raw data was then analyzed using the equations as described in section 1.2.2. to determine the stress-strain response of the specimens. The most important task in analyzing data was to reconstruct all the waves' origin in the same position as shown in Figure 32. After the alignment, the velocity, force transmitted to the specimen, strain rate, engineering stress, and engineering strain were calculated.

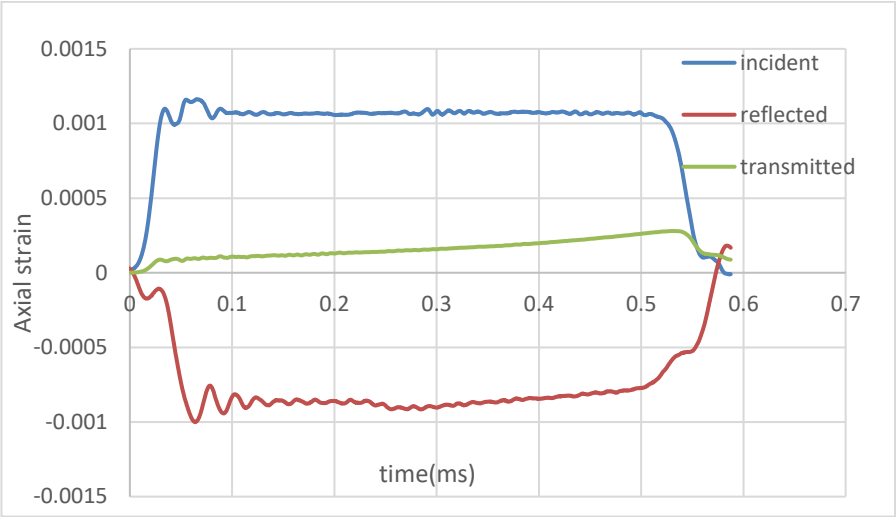

Figure 32: *Alignment of the waves*

The engineering stress(s) and engineering strain(e) are then converted to trues stress and true strain. True stress (σ)and true strain(ε) can be computed as:

$$\sigma = \frac{F}{A} \tag{1.38}$$

$$\varepsilon = ln\frac{L}{L_0} \tag{1.39}$$

where F is the load, L_0 is its initial length, A is the current cross-sectional area and L is the current gauge length.

For the compression tests, the volume conservation under plastic strains is assumed for metals. Engineering vs true measurements can be obtained using the following expressions (when compression is positive):

$$\varepsilon = -ln(1 - e) \tag{1.40}$$

$$\sigma = s\,(1 - e) \tag{1.41}$$

The high strain rate compression tests occur over a short duration of time and the heating changes from isothermal to adiabatic in nature. Hence, rapid temperature changes arise in the specimens during dynamic impact resulting in thermal softening. The kinetic energy absorbed by the specimen per unit volume (W) was determined by integrating the true stress-strain curve [67]:

$$W = \int_0^{\epsilon} \sigma \, \varepsilon \, d\varepsilon \tag{1.42}$$

Temperature rise is due to plastic deformation and it can be calculated from the following equation:

$$T_2 = T_1 + \frac{\beta}{\rho \, C_p} \int_0^{\varepsilon} \sigma \, d\varepsilon \tag{1.43}$$

where T_2 is the rise in temperature, T_1 = 297 K is room temperature, β is Taylor- Quinney coefficient, ρ is the density, 2830 kg/m^3 and C_p is specific heat capacity, 860 J/Kg K.

Here in equation (1.43) Taylor-Quinney coefficient is constant. However, previous works have shown that β is dependent on strain and strain rate in compression tests [67-69]. The value of β =0.85 was determined for the 7000 series aluminum alloy by Rouse et al. [69] and shown that the value of β does not depend on the strain rate for these aluminum alloys.

3. EXPERIMENTAL RESULTS

Cylindrical specimens with diameters of 5mm, 6mm, 8mm, 10 mm, and 12mm with L/D ratios of 0.6, 1 and 1.4 were tested in dynamic compression tests twice, with and without lubrication applied on the surface of the incident and transmitted bars. Also, the cuboid specimens with a square cross-section of 7mm sides and aspect ratios of 0.6, 1 and 1.4 were also tested. The stress-strain responses of specimens of different sizes are presented.

3.1 Tests without Lubrication

Figures 34-37 show the stress-strain curves at room temperature tested without lubrication between the specimen and pressure bars. All the experiments were carried with the same striker velocity of 8 m/s, but it can be clearly seen that the strain rate is not constant; it increases sharply and becomes uniform. It is observed that higher strain rates are obtained for smaller-diameter specimens of the same aspect ratio (Figure 33).

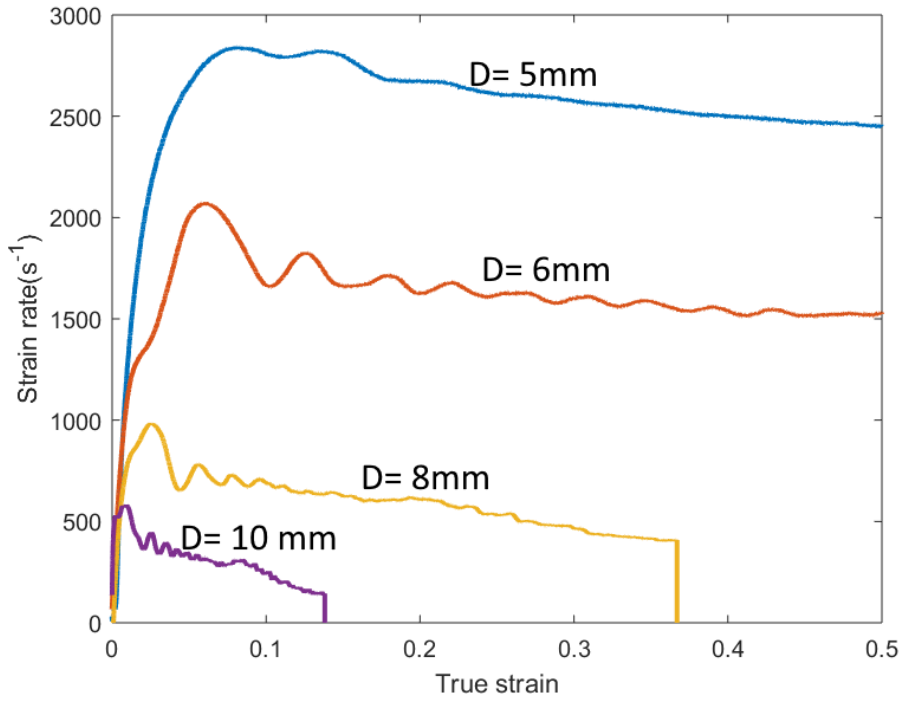

Figure 33: *Strain rates as a function of true strain for specimens of different diameters with the same aspect ratio of 0.6*

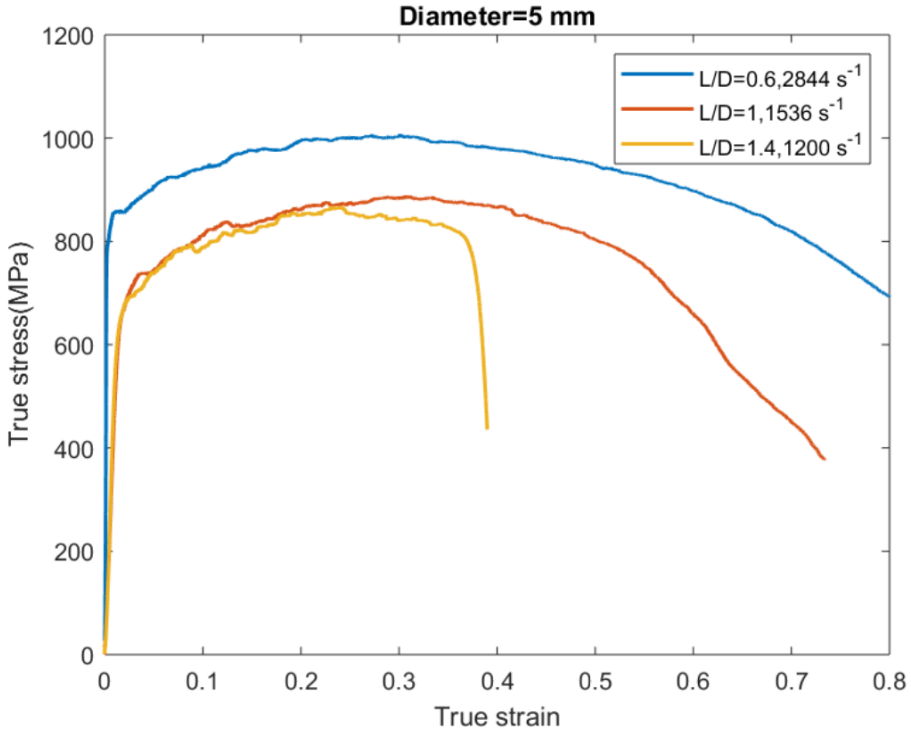

Figure 34:*Stress-strain curves of specimens with 5 mm diameter (unlubricated)*

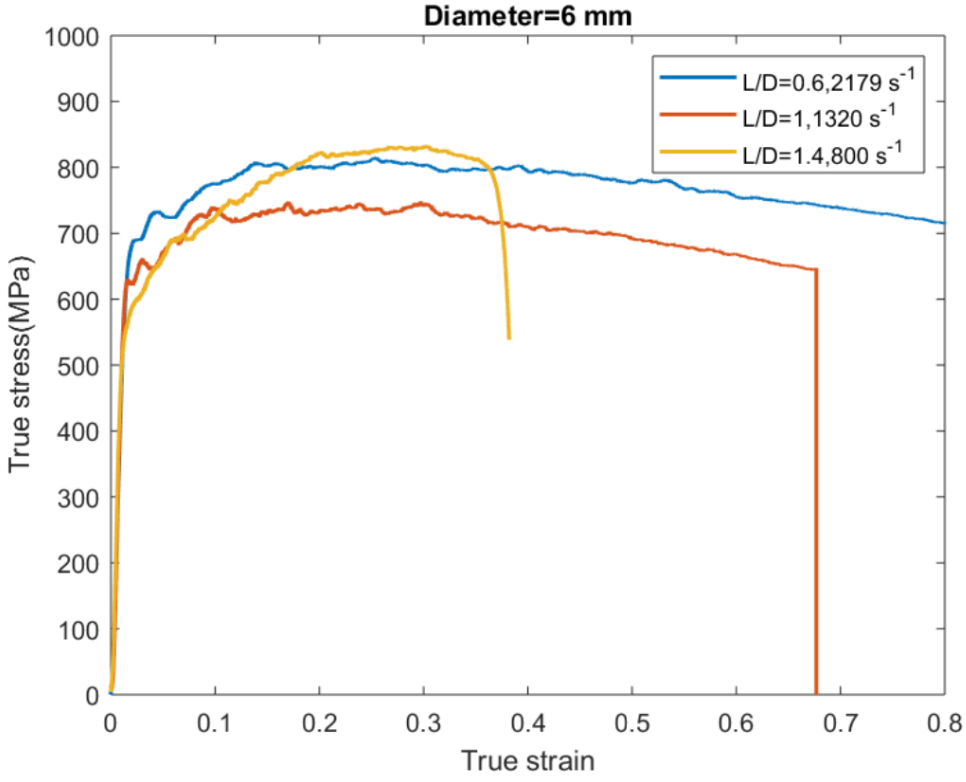

Figure 35: *Stress-strain curves of specimens with 6 mm diameter (unlubricated)*

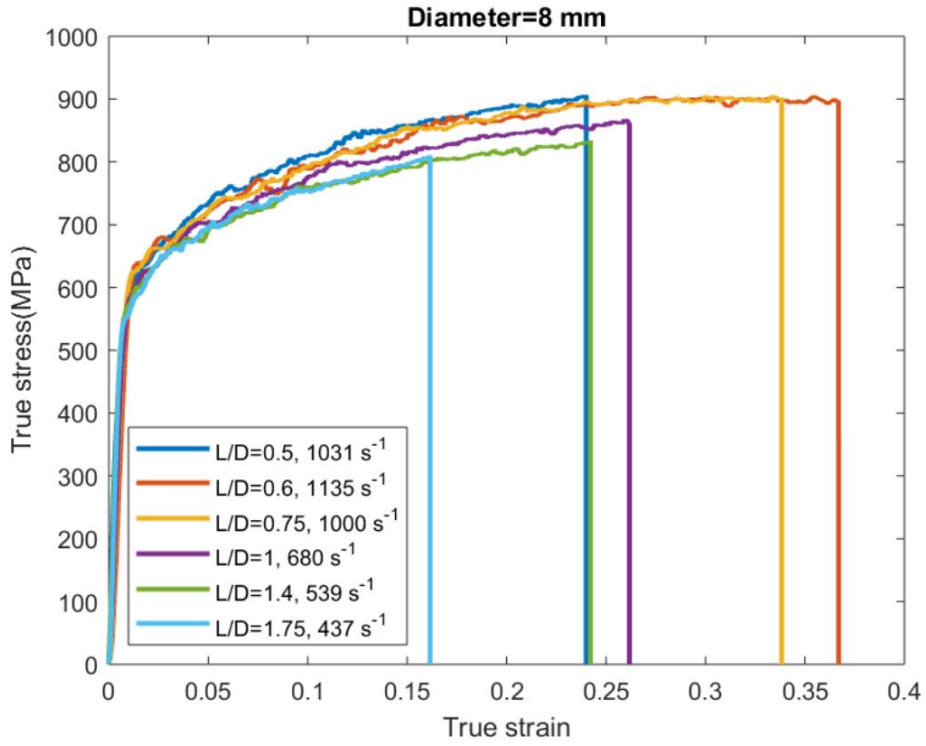

Figure 36: *Stress-strain curves of specimens with 8 mm diameter (unlubricated)*

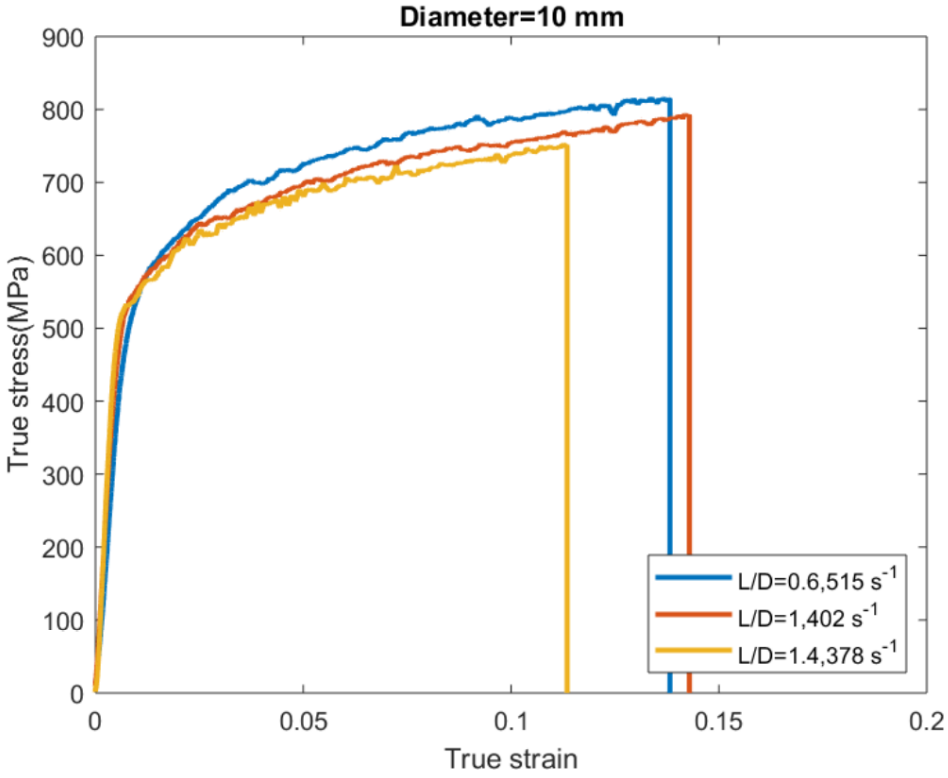

Figure 37: *Stress-strain curves of specimens with 10 mm diameter (unlubricated)*

From Figures 34 and 35, it can be seen that the yield stress is sensitive to strain rates above 1000 s^{-1}. The friction seems to affect the shorter specimen of the 5mm diameter specimen as the measured strength is much higher. On the other hand, the results in Figures 36 and 37 are obtained with specimen diameters of 8mm and 10 mm. The strain rate ranges from 300 s^{-1} to 1100 s^{-1} but similar dynamic mechanical characteristics are obtained. The yield stresses at these strain rates are nearly the same showing no significant difference in mechanical characteristics at intermediate strain rates and it can be said that this specimen size is reliable for dynamic testing.

It was not possible to get results with the specimens of 12 mm in diameter due to some technical difficulties with the strain gages. Hence, no conclusions are drawn from this specimen geometry. The strain rate decreases as the specimen size decreases and so this specimen size would be ideal for static tests rather than high strain rate tests.

3.2 Tests with Lubrication

The same experiments as presented in section 3.1 were repeated once again with the lubrication. The stress-strain responses of the cylindrical specimens with lubricant are presented in Figures 38- 41.

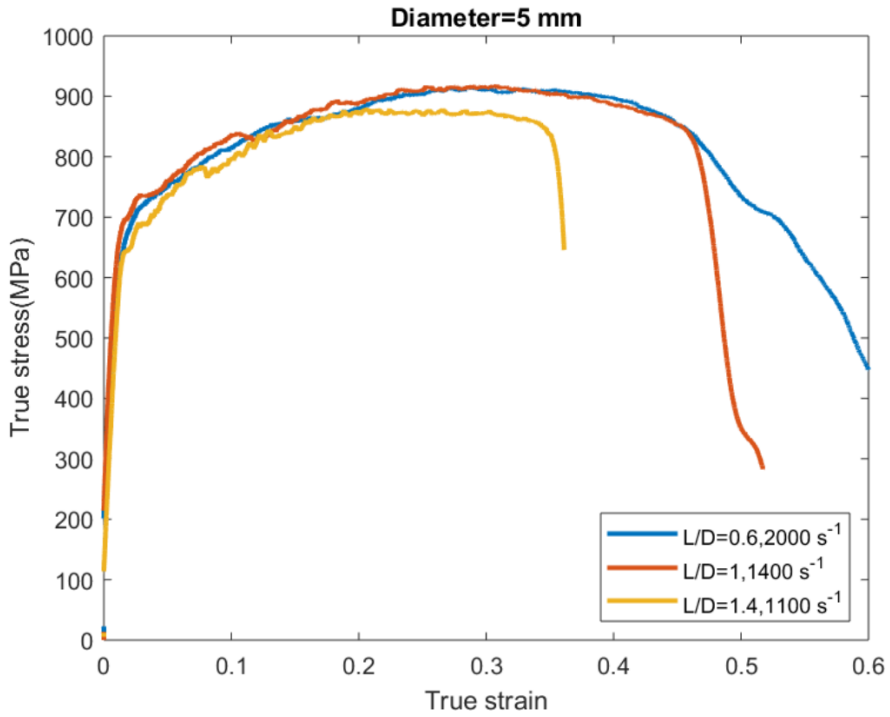

Figure 38: *Stress versus strain curves of 5 mm diameter specimens with lubricant*

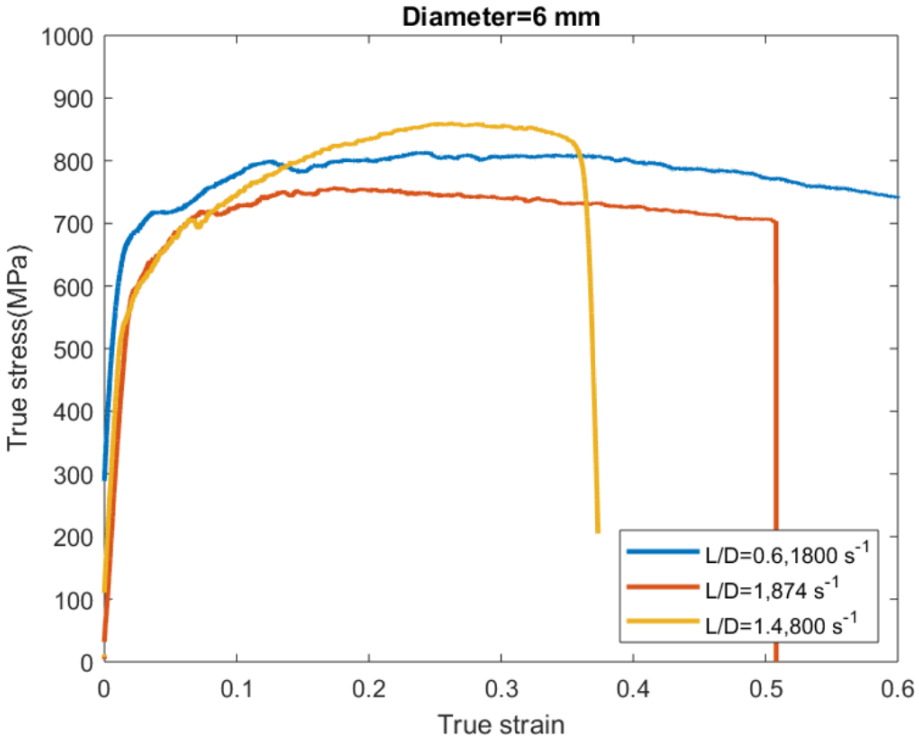

Figure 39: *Stress-strain curves of 6 mm diameter specimens with lubricant*

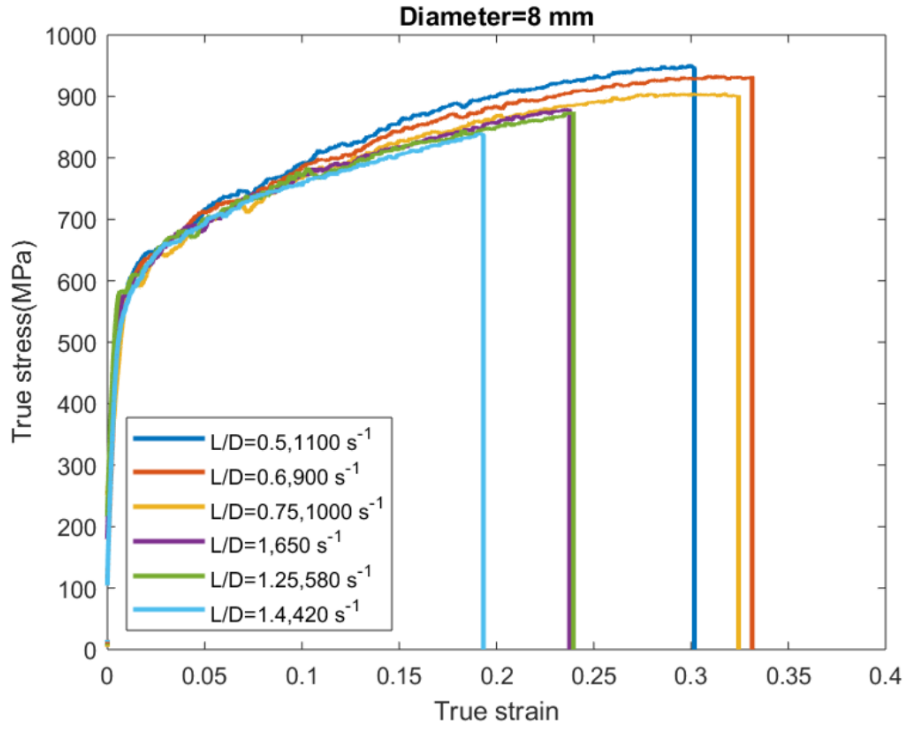

Figure 40: *Stress-strain curves of 8 mm diameter specimens with lubricant*

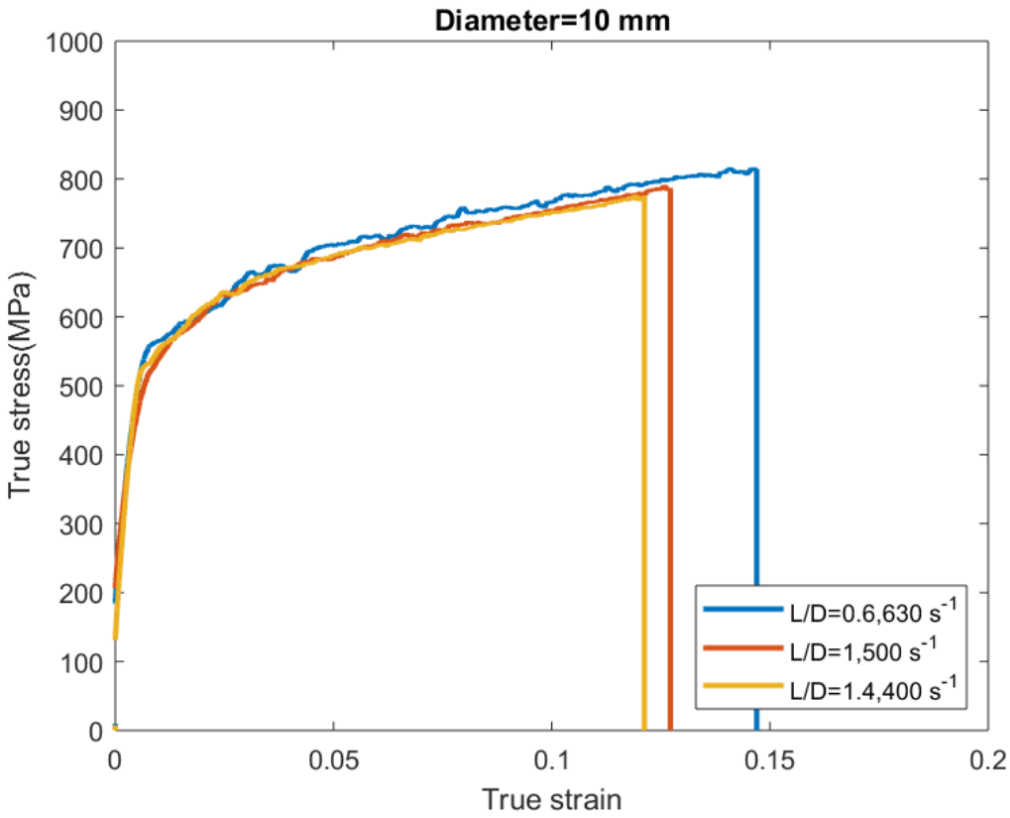

Figure 41: *Stress-strain response of 10 mm diameter specimens with lubricant*

The main difference that can be observed with the lubricated specimens is the decrease in the measured strength of the tested AA 7050-T351. This is clearly seen in the case of a 5 mm diameter specimen with an aspect ratio of 0.6. The stress-strain curves of 5mm and 6mm diameter lubricated specimens (Figures 38 and 39) with different aspect ratios demonstrate that the alloy is sensitive to higher strain rates above 1000 s^{-1}. The measured yield stress in both figures is similar at lower strain rates below at around 1000 s^{-1} but increases beyond the strain rates of 1000 s^{-1}. With larger diameters of 8mm and 10mm (Figures 40 and 41), we can see that there are no significant differences between the lubricated and unlubricated specimens. The yield stresses in all the cases are nearly the same, the only difference being the slight increment in the flow stresses at higher strain rates.

Now, to select the appropriate specimen size and length to diameter ratio, comparisons of experimental results obtained from the lubricated tests were made selecting the same aspect ratio of specimens with different diameters.

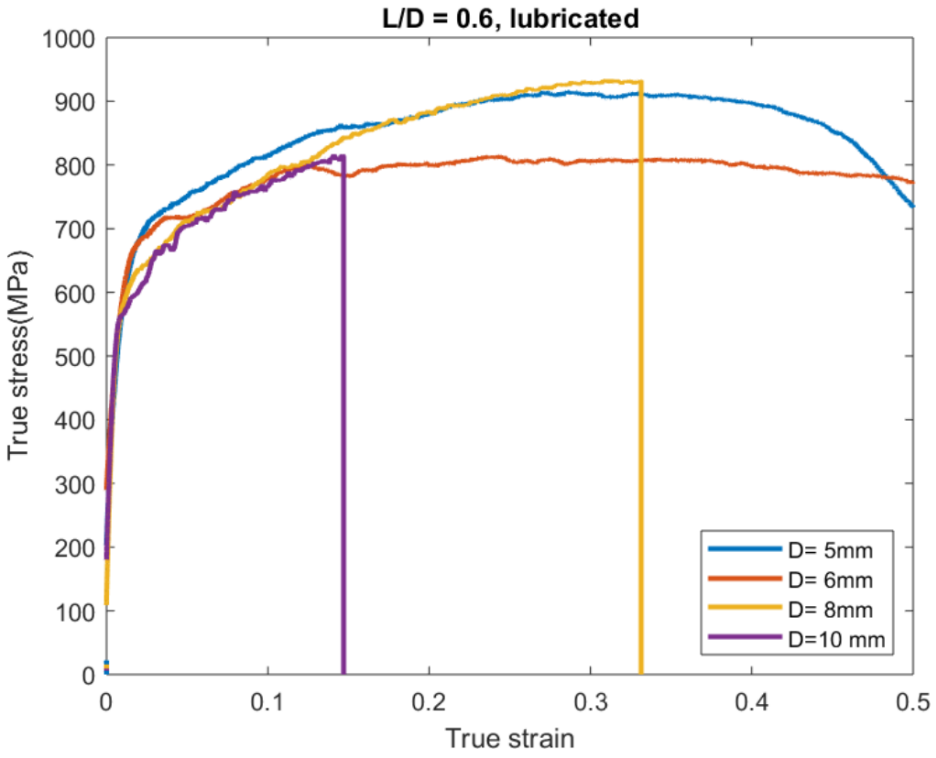

Figure 42: *Comparison of length to diameter ratio of 0.6 for the specimens with different diameters*

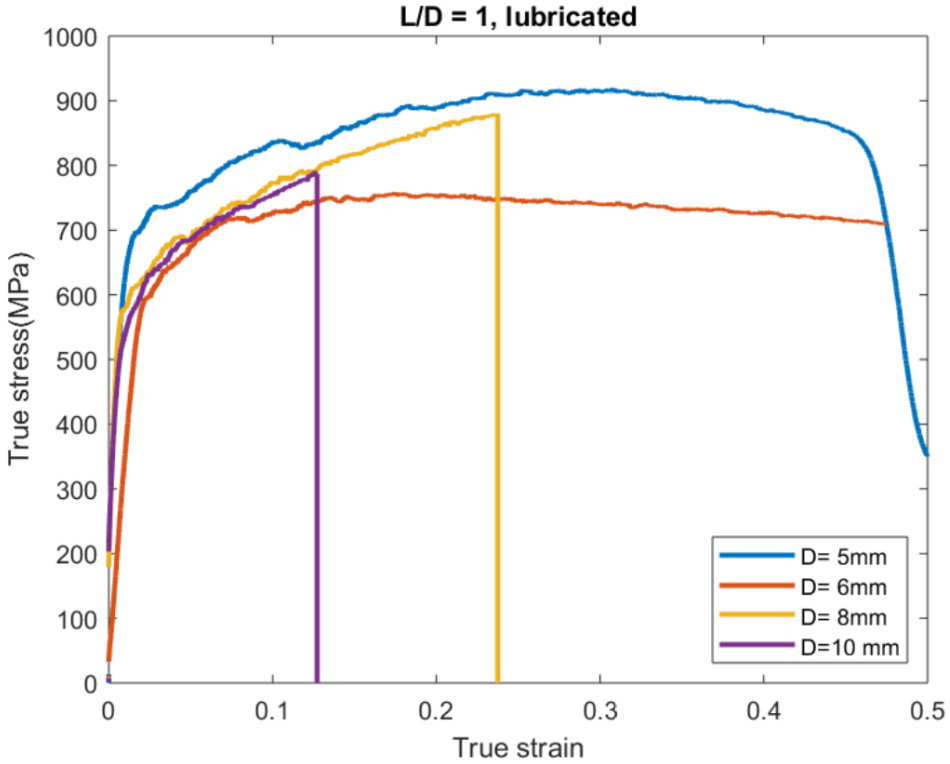

Figure 43: *Comparison of length to diameter ratio of 1 for the specimens with different diameters*

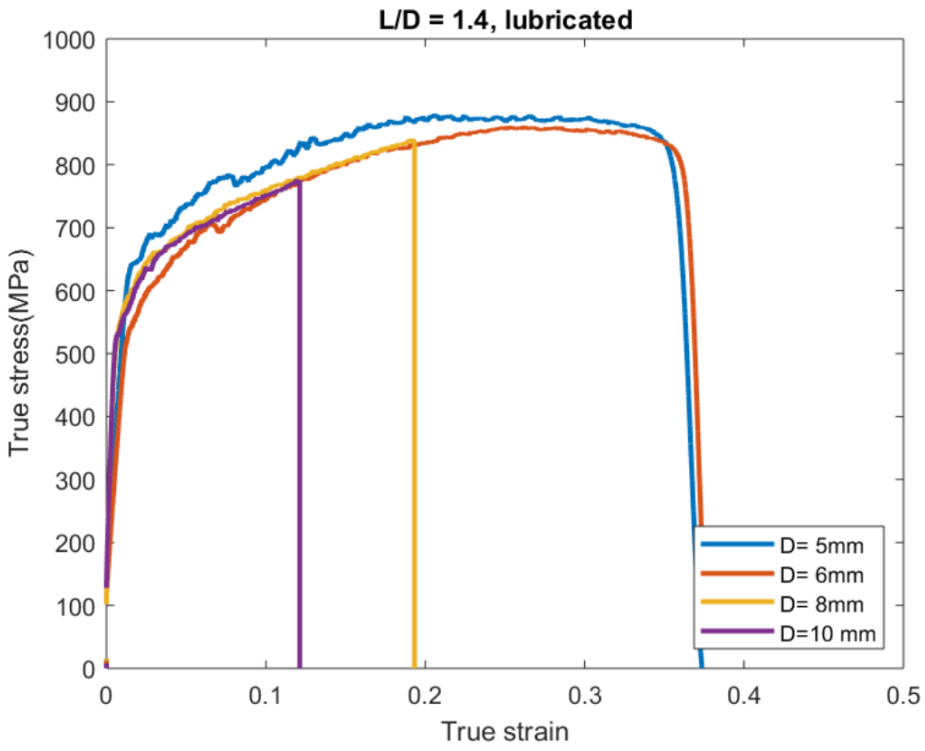

Figure 44: *Comparison of length to diameter ratio of 1.4 for the specimens with different diameters*

Figure 42 compares the stress-strain curves of specimens with different diameters and the same aspect ratio of 0.6. The curves are not identical because the strain rates are not the same for all the tested specimens. Higher strain rates of nearly 2000 s^{-1} are obtained with the specimens of diameters 5 mm and 6 mm whereas larger specimens of 8mm and 10 mm exhibit strain rates lower than 1000 s^{-1}. Moreover, higher yield stress is observed for specimens with diameters of 5mm and 6mm as compared with 8mm and 10 mm diameter specimens which show that yield stress increases with strain rates.

On the other hand, the higher yield stress is obtained only with a 5 mm diameter specimen for the aspect ratio of 1 and 1.6 as seen in Figures 43 and 44. This is because the strain rate above 1000 s^{-1} is obtained with a 5 mm diameter specimen with these aspect ratios, whereas other specimens with diameters of 6mm, 8mm and 10mm give strain rates less than 1000 s^{-1}. So, we can say that this AA 7050-T351 exhibits higher strain rate sensitivity above 10^3 s^{-1} as discussed in section 1.5. Hence, the most suitable specimens for dynamic mechanical testing, in this case, are with the diameters between 6mm-10 mm with aspect ratios of 0.6-1.4 and with the lubrication between the specimens and pressure bars.

3.3 Comparison between Lubricated and Unlubricated Tests

As discussed earlier, the main differences between the lubricated and unlubricated specimens can be clearly observed with a shorter specimen of 5 mm in diameter. The difference in the stress-strain curve of the lubricated and unlubricated specimens is illustrated in Figure 45. The high frictional effect is observed with a smaller aspect ratio whereas larger aspect ratios are not largely influenced by the friction. With the bigger specimens of 8mm and 10 mm, the frictional effect does not bring larger variations in results. To obtain the material parameters using the JC-model lubricated specimens were used.

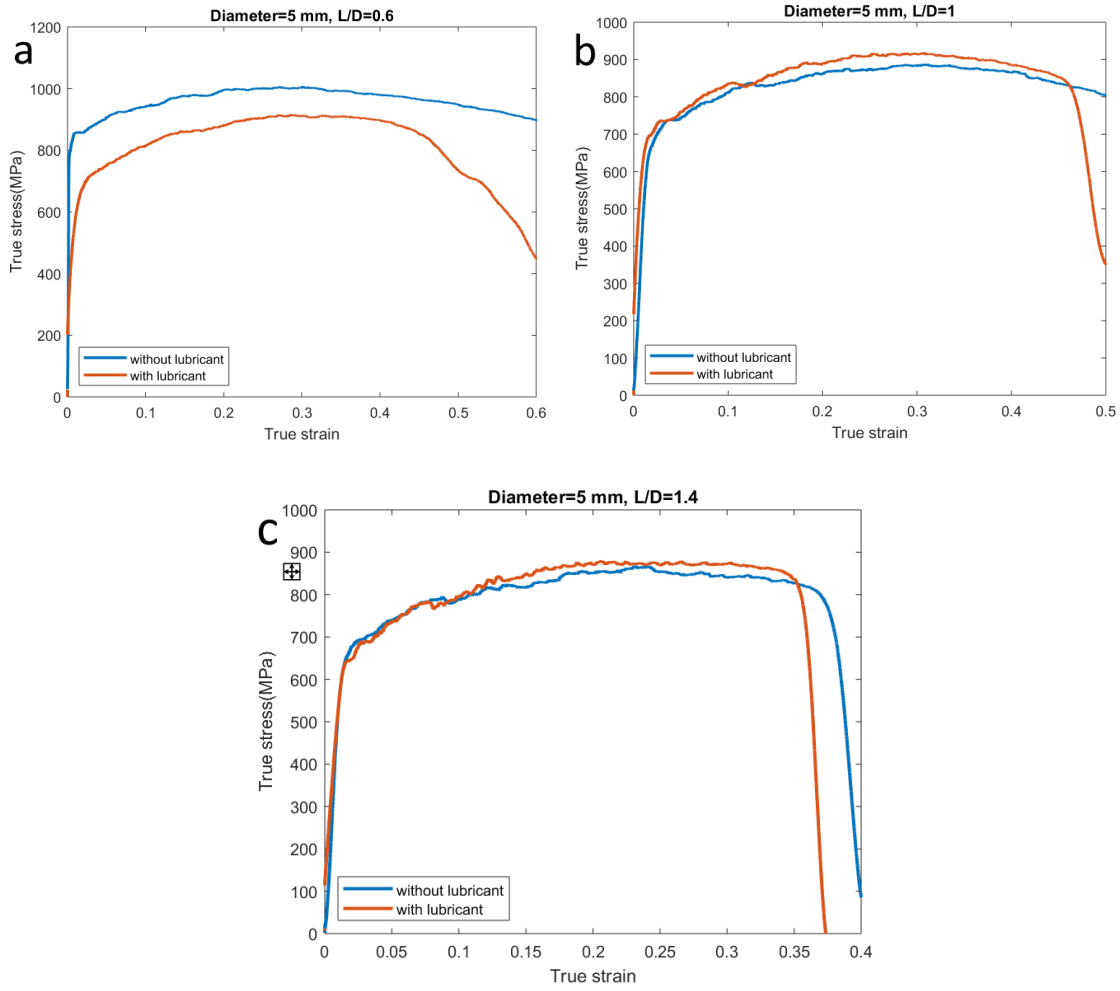

Figure 45: *Influence of lubrication on dynamically tested specimens*

During the high strain rate compression tests, part of the energy used in the deformation of the specimens converts into heat and increases the temperature of the specimens. The increase in temperature of the specimens was estimated using equation (1.43). The increase in temperature of the specimens in the dynamic tests performed with and without lubrication are compared in Figure 46. In both cases, ΔT increases with strain. However, when high friction exists between the specimen and the pressure bar, the increase

in temperature of the specimen is also high. So, lubrication is essential in the dynamic tests to avoid the miscalculation of measured strength as well as the adiabatic heating of the specimens.

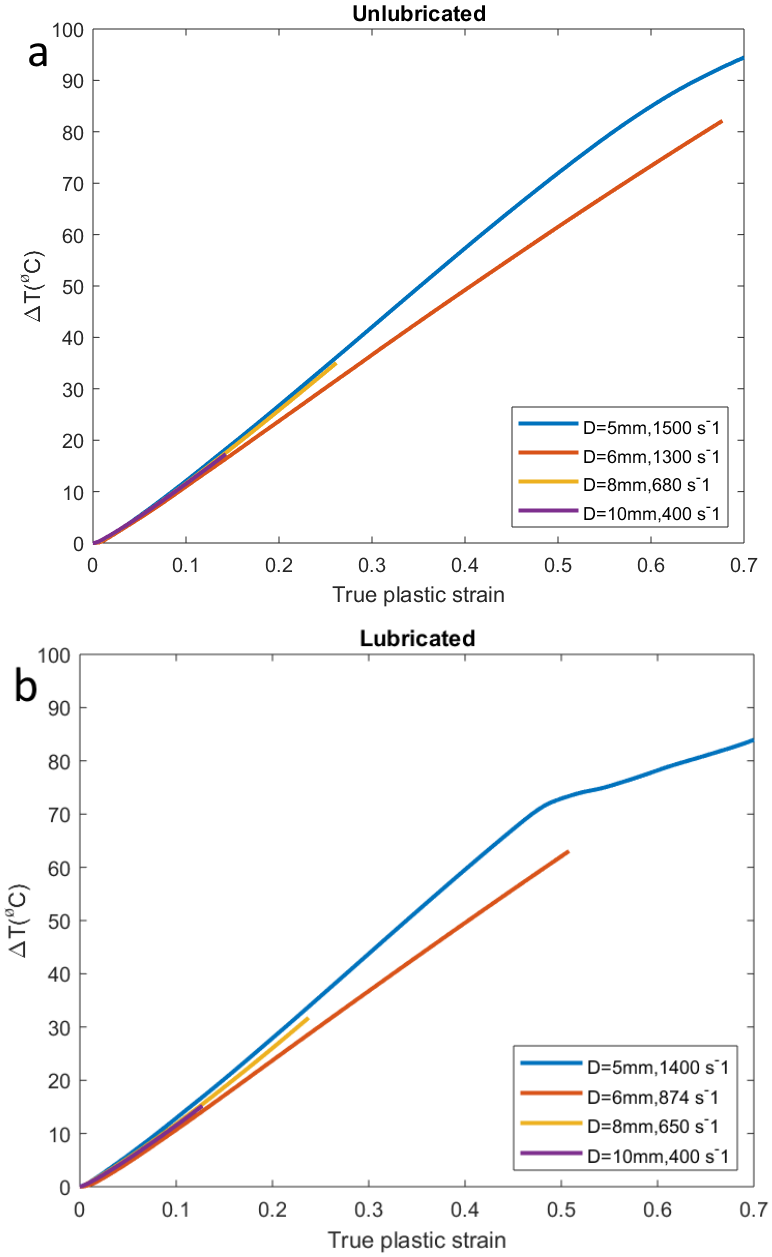

Figure 46: *Temperature increase (ΔT) as a function of true plastic strain at different strain rates; (a) unlubricated specimens and (b) lubricated specimens*

3.4 Tests with Cuboid Specimens using Lubricant

The cuboid specimens having a square cross-section with 7mm sides and different lengths were also tested. To confirm the compatibility of cuboid and cylindrical specimens, both specimens with similar cross-sectional area and aspect ratio were compared. From Figure 48, it can be observed that the stress-strain response of AA 7075-T351

differs while using two different types of specimen configurations. The extensive study of cuboid specimens has been done by Zhong et al. [53] and they mentioned that the deformation is not uniform as high level of stresses were concentrated on the corners of cuboid specimens. Hence, this type of specimen should be discarded.

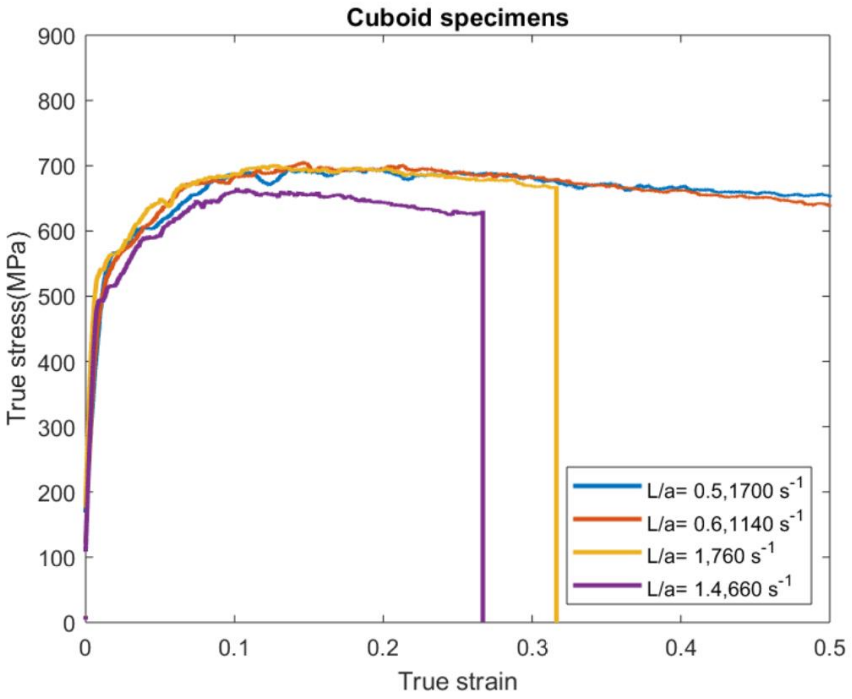

Figure 47: *Stress-strain response of cuboid specimens (Here, L is the length and a represents sides of square cross-section)*

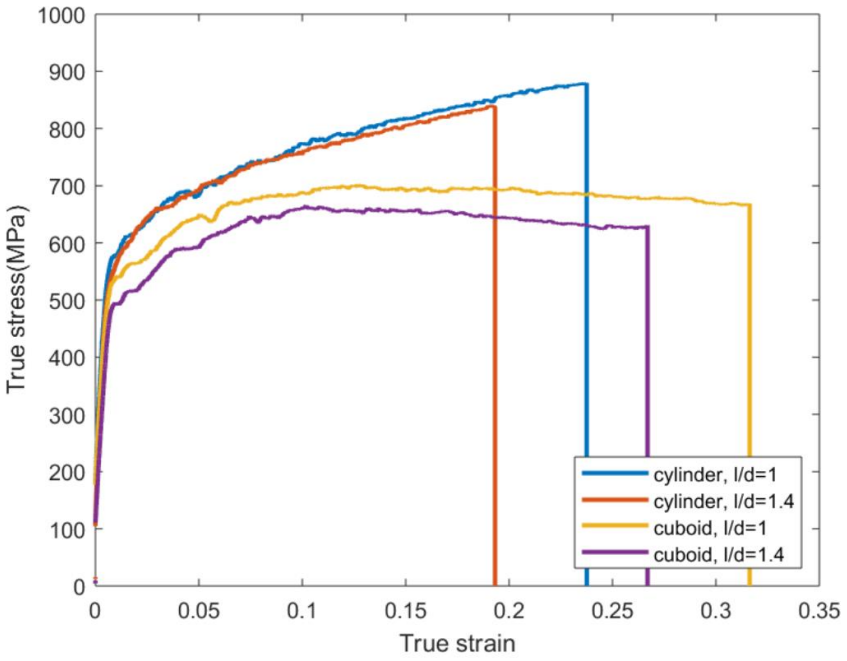

Figure 48: *Comparison between cylindrical and cuboid specimens*

3.5 Determination of JC-model Parameters

The JC- model material parameters in the constitutive equation (1.26) can be determined based on the experimental results by using the following steps:

(1) At a reference strain rate and reference temperature, the Eq. (1.26) will reduce to:

$$\sigma = (A + B\varepsilon^{n}) \tag{1.44}$$

Normally the value of A is calculated from the quasi-static test at a reference strain rate.

(2) Taking logarithm on both sides of the equation (1.44), we will get:

$$ln(\sigma - A) = ln\, B + n\, ln\, \varepsilon \tag{1.45}$$

The value of A and flow stress at various strains can be substituted in Eq. (1.45), then ln(σ-A) vs. ln ε can be plotted. The intercept of the fitting line gives the value of B while n is the slope of the line.

(3) At a reference strain rate and reference temperature Eq. (1.26) can be written as:

$$\frac{\sigma}{(A+B\varepsilon^{n})} - 1 = \text{C ln}\dot{\varepsilon}^{*} \tag{1.46}$$

The slope of the curves obtained by plotting $(\frac{\sigma}{(A+B\varepsilon^{n})} - 1)$ vs $\ln\dot{\varepsilon}^{*}$ gives the value of C.

The above-explained procedure is widely used to determine the JC-model parameters, but this was not exactly followed in this case. All the tests were performed at room temperature and the JC- model parameters were calculated by simply fitting the experimental stress-strain curves performed under different strain rates and taking 1000 s^{-1} as a reference strain rate. Although the tests were performed at room temperature, the value of 'm' was also determined by calculating temperature data from the adiabatic heating as explained below.

Basically, the value of 'm' can be derived if the experiments are performed at high temperatures. But it is also possible to estimate the value of 'm' even in a small range of temperatures. As shown before in Figure 46, the SHPB experimental tests are adiabatic where it implies that the temperature of the specimens increases. So, in order to fit the JC-model to the experimental data, we also need to introduce thermal softening in the model. For that, we need only two parameters of the JC-model: T_{melt} and m. If these parameters are not introduced in the fitting process, isothermal curves are obtained instead of the adiabatic curves.

Hence, in this case, although the experiment was done only at room temperature, the value of the parameter ‘m’ was derived simply by introducing the parameters to fit the SHPB experimental curves in the excel file showing the best agreement with some value of ‘m’. With this procedure, we are just adjusting the value of ‘m’ for the range of temperatures from room (reference) temperature to the temperature at the end of the tested sample. The final parameter values of A, B, n, m, and C obtained by fitting are shown in Table 5.

The comparison of the stress-strain curves calculated with the JC-model and experimental data is shown in Figure 49. Normally, the stress-strain curve calculated with the JC model does not include the elastic part, but the elastic strain was also calculated in this case. The fitted curve does not agree with the experimental results of 5 mm and 6 mm diameters but agrees well with the results of 8 mm and 10 mm diameter specimens. Then, these parameters were later used in the numerical simulations.

Table 5:*Johnson-Cook parameters of AA 7050-T351*

$\sigma = (\mathrm{A} + \mathrm{B}\varepsilon^{\mathrm{n}})(1 + \mathrm{C}\ln\dot{\varepsilon}*)(1 - \mathrm{T}^{*\mathrm{m}})$				$T^* = \frac{T - T_{ref}}{T_{melt} - T_{ref}}$
A(MPa)	B(MPa)	n	C	m
490	735	0.39	0.017	1.52

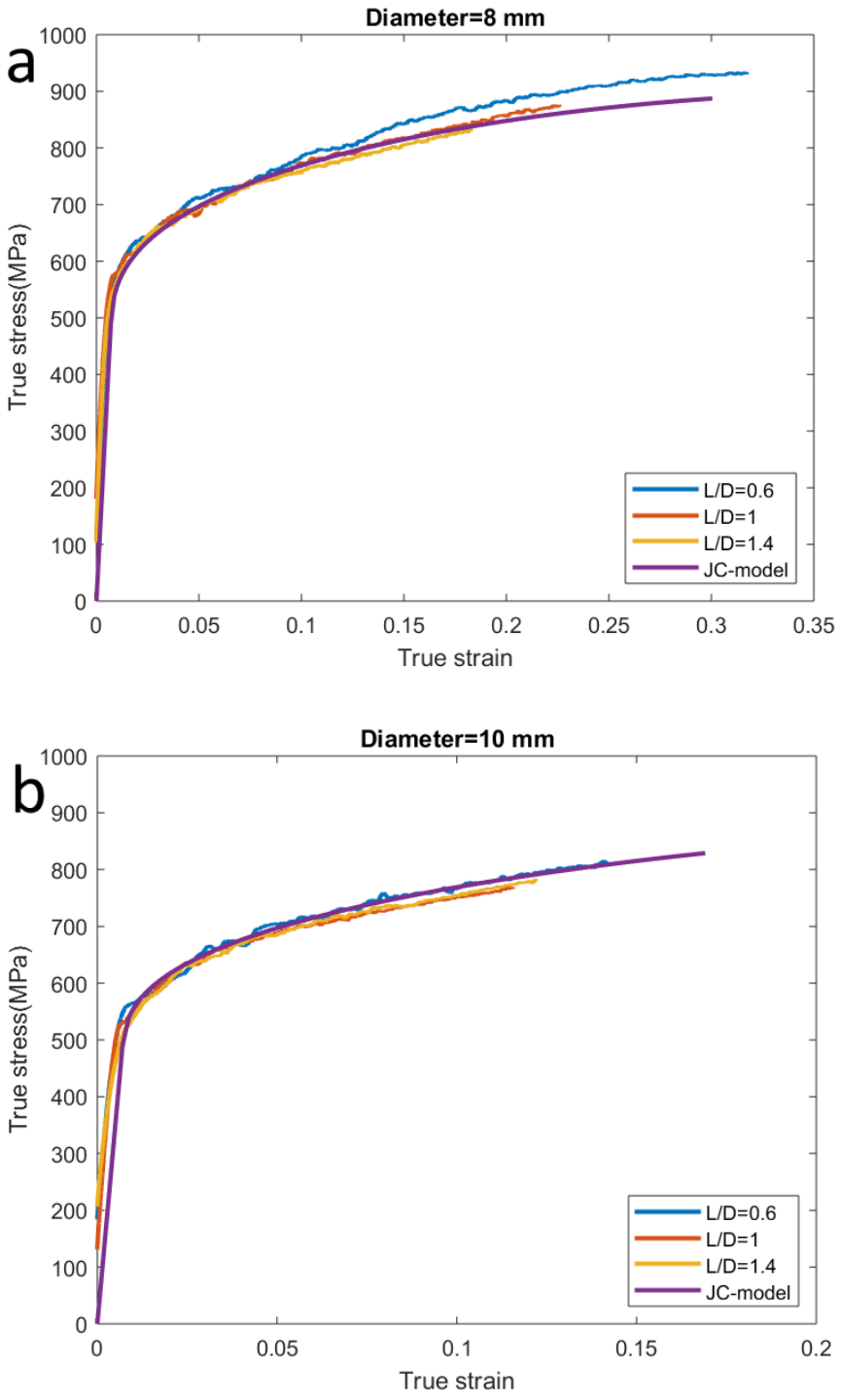

Figure 49:*Comparison of stress-strain curves calculated with JC-model to the experimental data (a) 8mm ;(b) 10 mm*

4. NUMERICAL SIMULATIONS

Numerical simulations were performed using LS-Dyna, which is a finite element program for nonlinear dynamic analysis. 2D axisymmetric-model in the y-axis was used. The main reason to use the axisymmetric 2D model is to reduce the computation time. The exact dimensions of the projectile, incident and transmitted bars as in the laboratory were used to construct a 2D model in the simulation. The graphical representation of the simulation is illustrated in Figure 50.

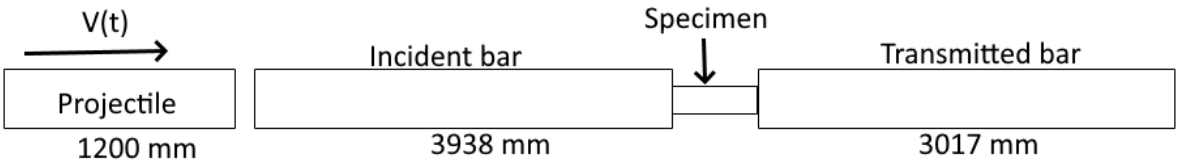

Figure 50: *Graphical representation of numerical simulation*

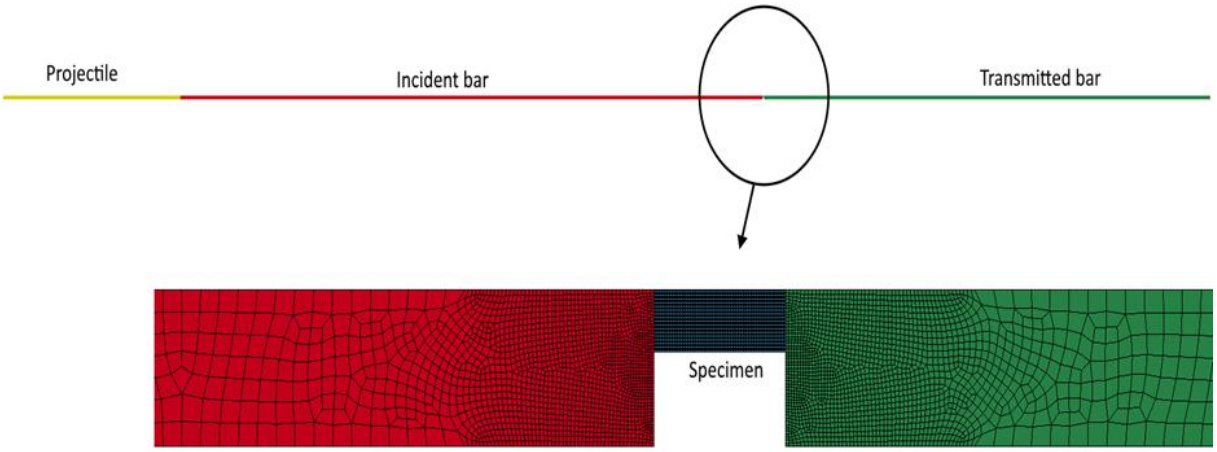

Figure 51: *2D-axisymmetric finite element model in the y-axis*

Figure 51 shows the 2D-axisymmetric model that had four parts: specimen placed between the incident bar and transmitted bar and the projectile to generate the stress waves. It is well known that mesh sensitivity has a tendency to decrease with smaller mesh size and reasonable mesh size should be selected for accurate results [70-72]. The element size dependence of the Johnson-Cook dynamic failure model has been studied by Goran et al. [72] using element sizes of 0.1,0.3,0.5 and 1 mm. They studied

mesh dependence based on the results of force-displacement curves and accurate results were obtained with a finer element size of 0.1mm.

The bars and specimen were modeled using a structured mesh by selecting 4 edges. The size of the elements was 0.1 mm in the specimen. Also, a fine mesh of 0.1 mm size was used at the end and beginning (20 mm to be exact) of the incident bar and transmitted bar respectively. On the other hand, the coarse mesh of size 2 mm was used in other parts of the bars and projectile. The number of elements used in the projectile, incident bar, and transmitted bar was 3600,13443 and 10675 respectively. The number of elements of specimen varied with length to diameter ratio. For example, 5 mm diameter and 3 mm long specimen had 900 elements.

Axisymmetric solid (y-axis of symmetry)-volume weighted shell elements were defined for all the defined parts. Two different kinds of material properties were defined for the used bars and the specimen. 001_ELASTIC with material properties listed in Table 4 were assigned to the projectile and pressure bars and 015_JOHNSON_COOK with properties listed in Tables 3 and 5 were assigned to specimen. The reference strain rate of 1000 s^{-1}, shear modulus of 27 GPa and bulk modulus of 58 GPa were also used to define the properties of the specimen.

Equation of state is required to simulate material behavior accurately. EOS_LINEAR_POLYNOMIAL was used to simulate bulk behavior by setting C1 to bulk modulus and all other C terms to zero. EOS can only be defined to shell element and recommended if the strain rates are low to moderate.

The velocity of 8 m/s (same as in the experiments) in y-direction was set to a projectile. Then, a 2D-dimensional contact was defined between all the parts with both static and dynamic coefficients of friction. Different coefficients of friction were set to compare the simulated true stress-strain curves with the experimental curves. The computational time of the dynamic simulation was set in the CONTROL_TERMINATION menu. The end time of 2.5 milliseconds was used. The von-mises stress distribution in one of the simulations is presented in Figure 52 below.

(a)

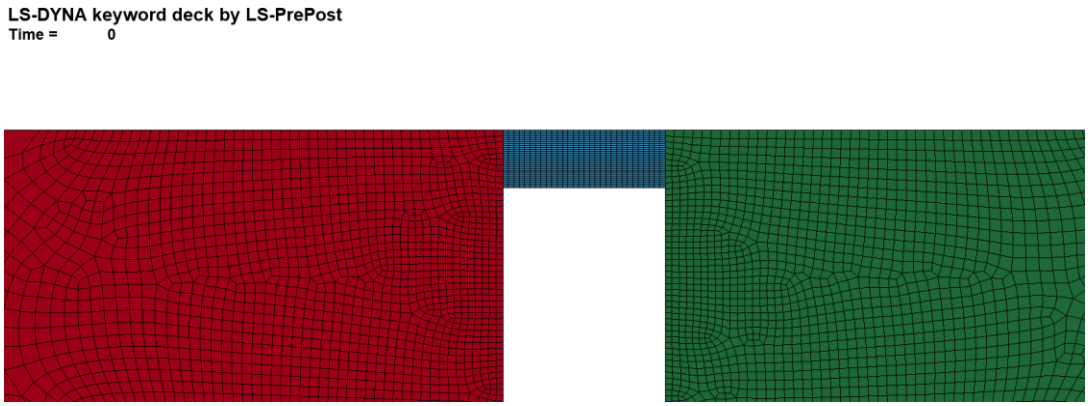

(b)

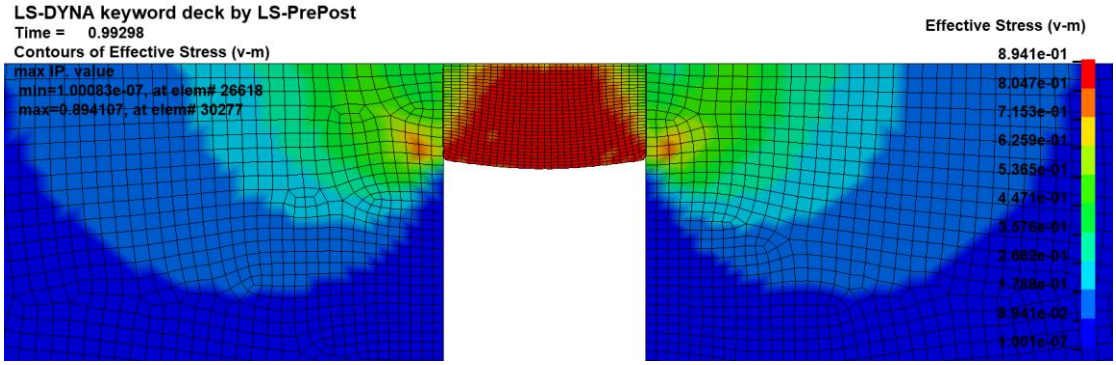

(c)

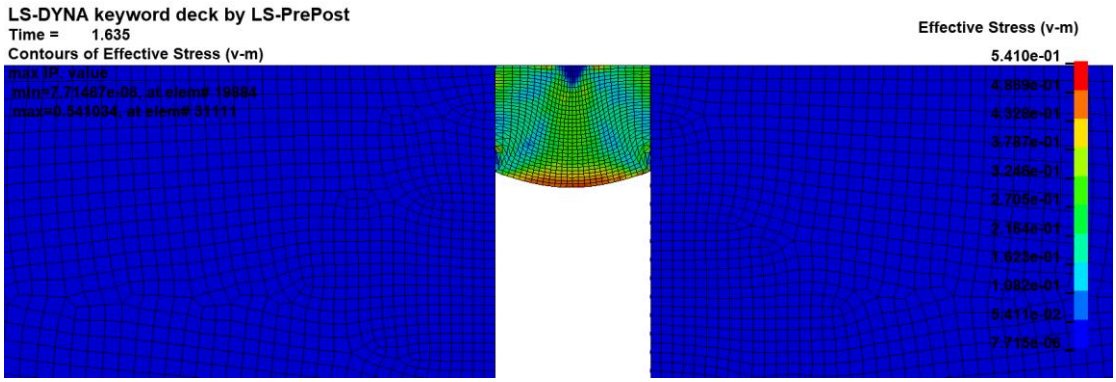

Figure 52: *Von-mises stress at (a) t=0 ms, (b) t=0.9 ms and (c)t= 1.6 ms*

Figure 53 shows the simulated stress waves in y-direction that were measured in the middle section of the bars. The procedure to obtain the stress-strain response of the simulated material is similar to the experiments described in section 1.2.2.

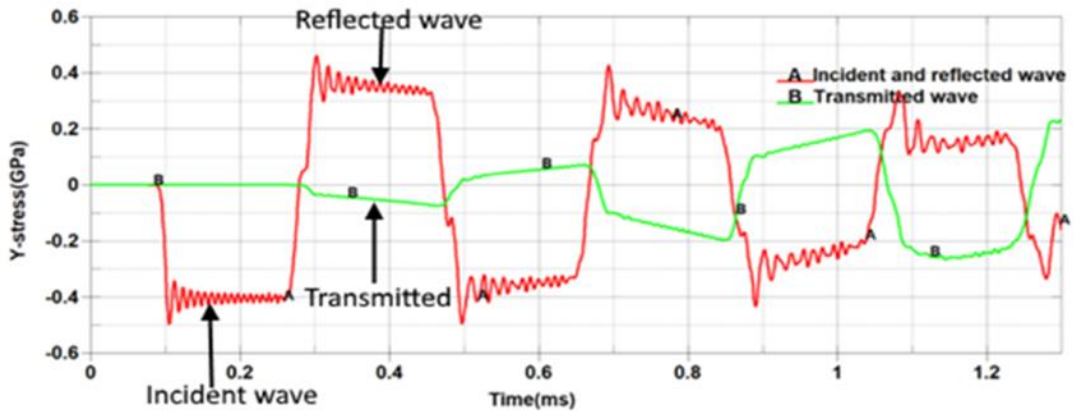

Figure 53: *Simulated waves measured at the middle of the pressure bars*

4.1 Simulation Results

Simulations were carried out using different coefficients of friction and compared with the experimental results. The results of the axial strain obtained from the incident and transmitted bar presented in Figure 54 reveal that the friction coefficient affects the reflected and transmitted stress waves. The highest reflected stress wave is recorded when there is no friction between the bars and the specimen, and it decreases. Likewise, the transmitted stress waves increase significantly with friction.

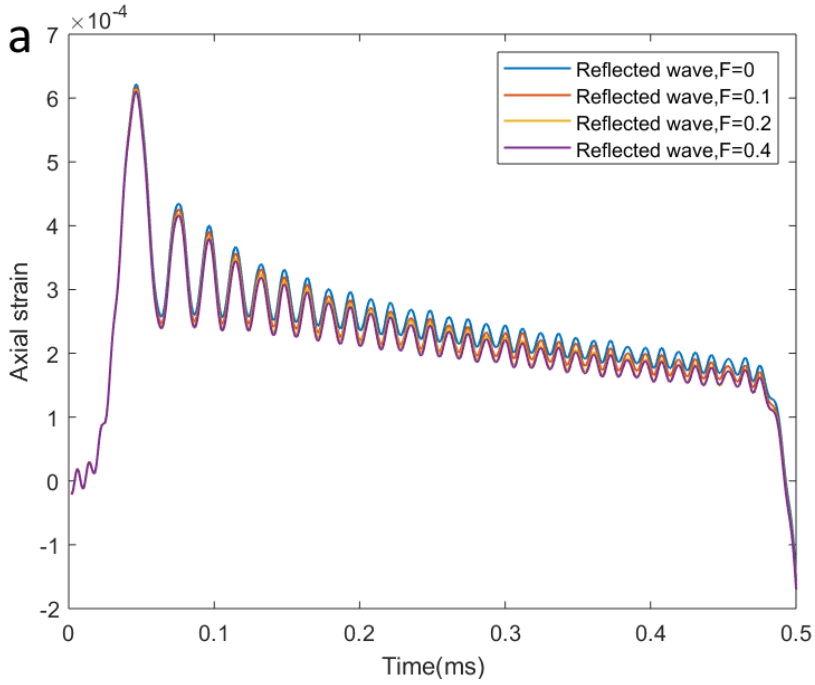

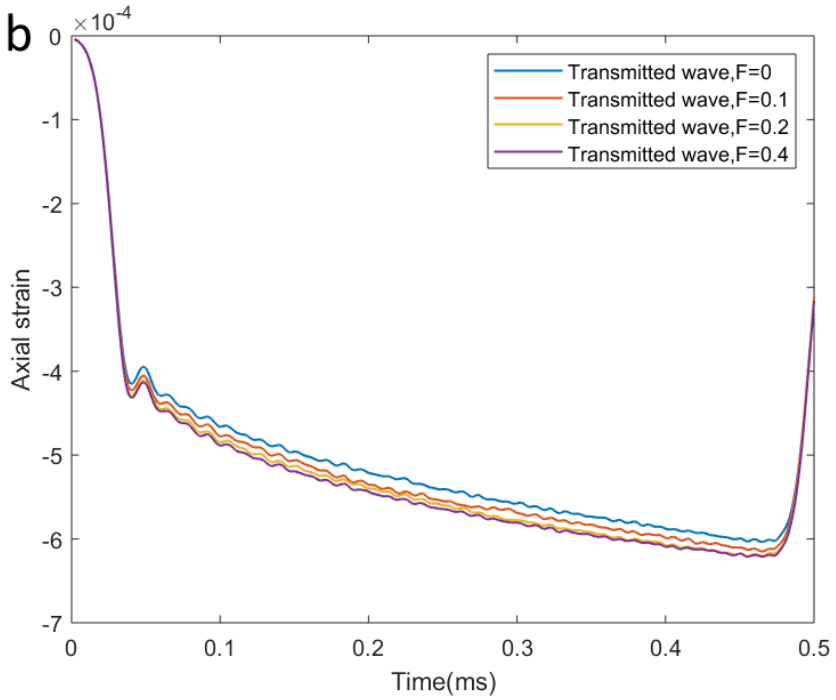

Figure 54: *Comparison of (a) reflected stress waves and (b) transmitted waves under different coefficients of friction*

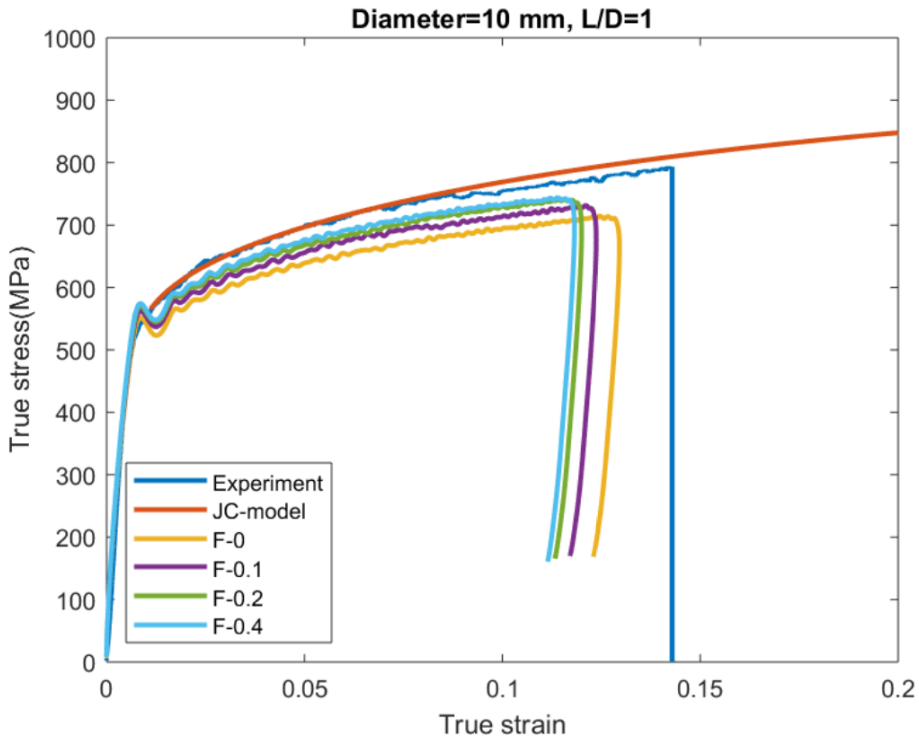

Figure 55:*Comparison of the experimental stress-strain curve with the JC-model, and simulations with different coefficients of friction of 10 mm diameter with an aspect ratio of 1*

The comparison of experimental results of 10 mm diameter specimen with an aspect ratio of 1 and numerical simulations performed using different coefficients of friction, μ=0,

0.1, 0.2 and 0.4 is illustrated in Figure 55. The yield stress obtained with μ= 0 matches the experimental results but the plastic curve does not match. Both the yield stress and flow curve increase with coefficients of friction.

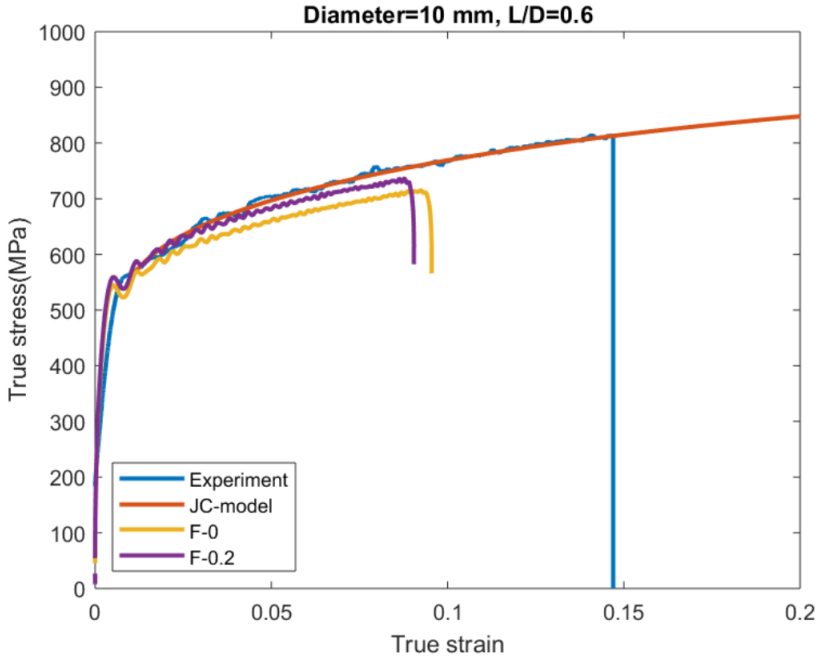

Figure 56: *Comparison of the experimental stress-strain curve with the JC-model, and simulations with different coefficients of friction of 10 mm diameter with an aspect ratio of 0.6*

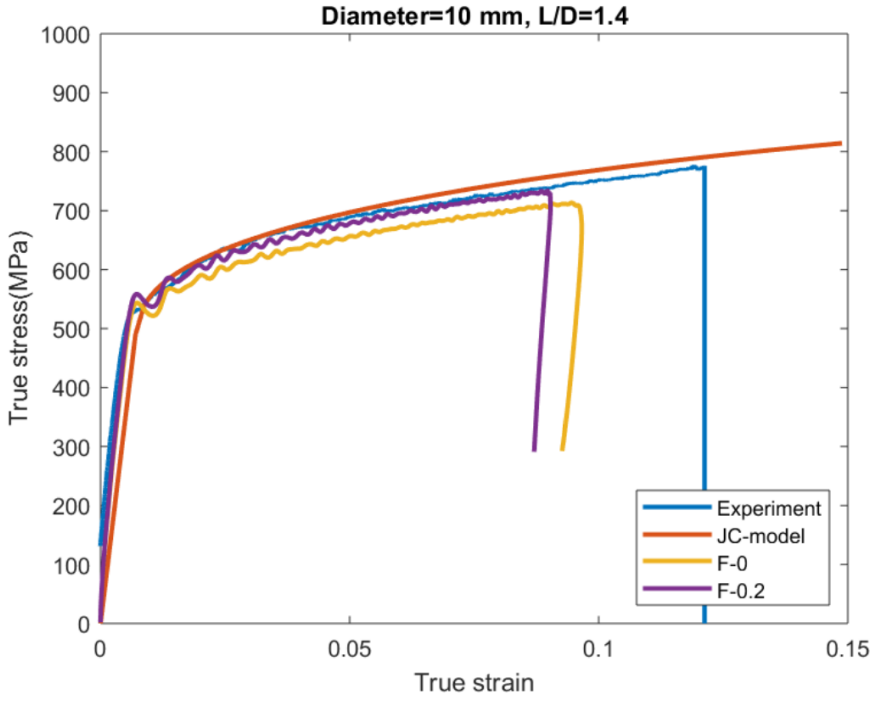

Figure 57: *Comparison of the experimental stress-strain curve with the JC-model, and simulations with different coefficients of friction of 10 mm diameter with an aspect ratio of 1.4*

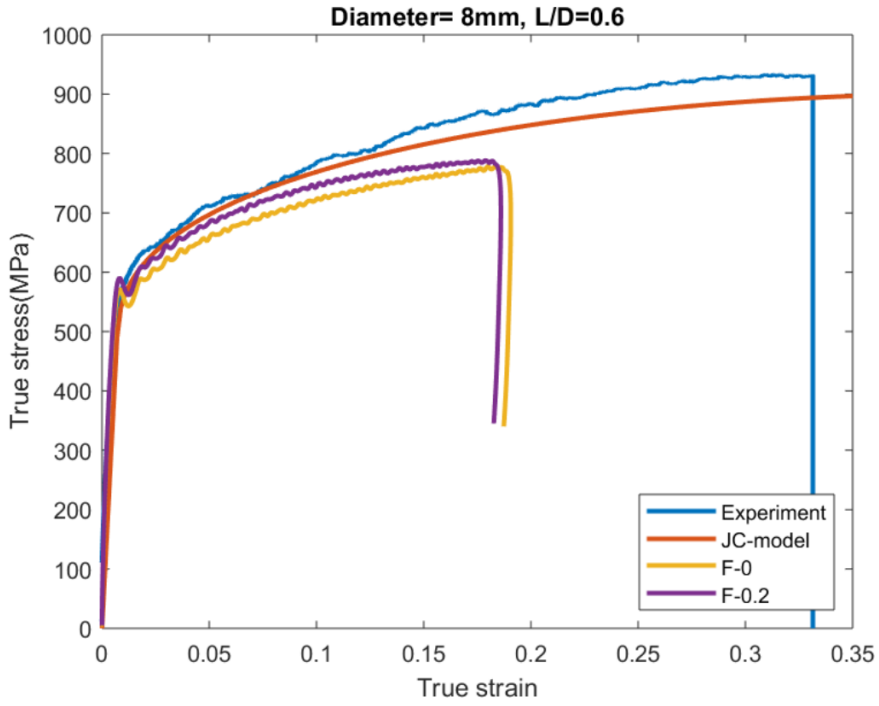

Figure 58: *Comparison of the experimental stress-strain curve with the JC-model, and simulations with different coefficients of friction of 8 mm diameter with an aspect ratio of 0.6*

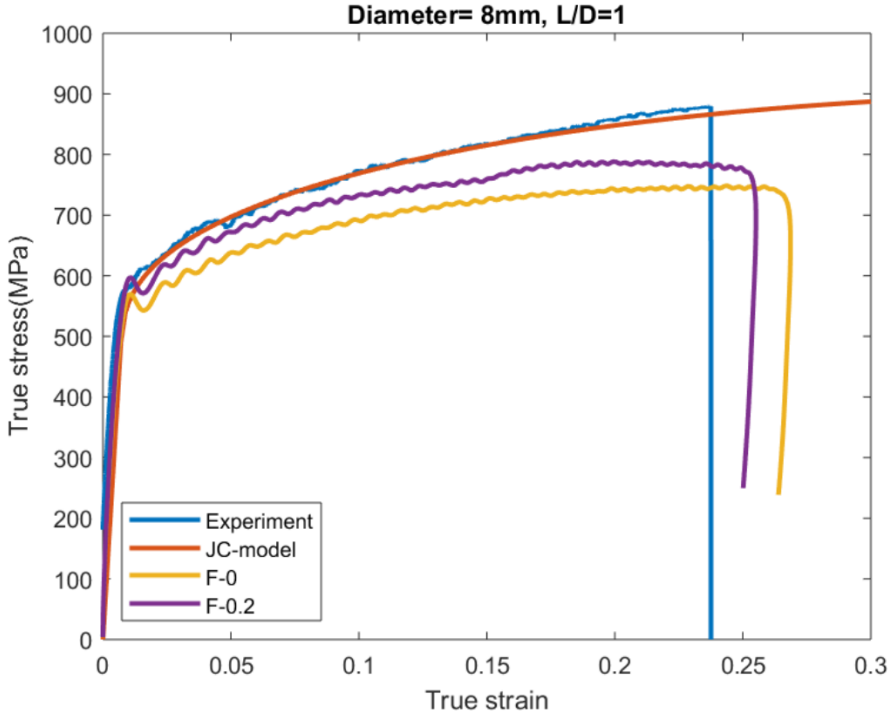

Figure 59: *Comparison of the experimental stress-strain curve with the JC-model, and simulations with different coefficients of friction of 8 mm diameter with an aspect ratio of 1*

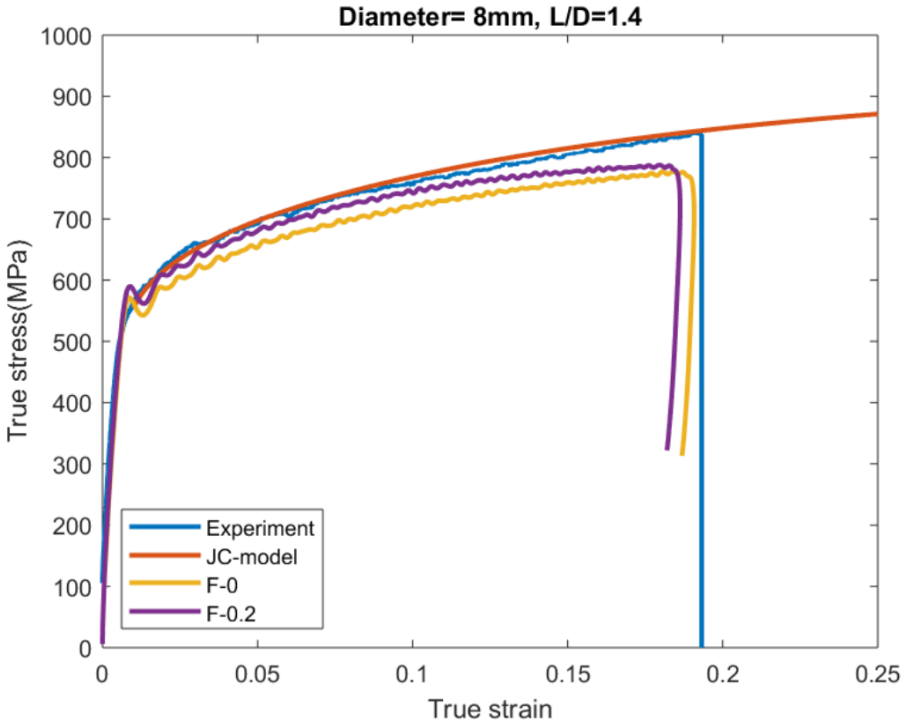

Figure 60: *Comparison of the experimental stress-strain curve with the JC-model, and simulations with different coefficients of friction of 8 mm diameter with an aspect ratio of 1.4*

The numerical simulations carried out using both the 8 mm and 10 mm specimens show similar results. The most accurate results, when compared with the experimental results, were obtained using the length to diameter ratio of 0.6 and 1.4 in all the cases.

5. DISCUSSION

The effects of specimen geometry, lubrication, and strain rate on the compressive properties of aluminum alloy 7050-T351 were investigated in this study. To investigate the effects of friction, experiments were conducted with and without the presence of lubrication. By comparing the Figures in sections 3.1 and 3.2, we can conclude that the shorter specimen (aspect ratio, L/D= 0.6) with a smaller diameter of 5 mm is sensitive to lubrication. However, the longer specimens (L/D =1 and 1.4) are not greatly affected by the lubrication between the specimen and pressure bars. Similar results have been reported by Li et al. [62] where they tested the lubricated and unlubricated specimens with 3.5 mm diameter using aspect ratios of 0.4, 1 and 1.4. And in the case of the bigger specimens with diameters 6 mm, 8 mm and 10 mm, the friction does not greatly affect the experimental results for all the aspect ratios. The measured stress-strain curve obtained with unlubricated specimens for all the aspect ratios, L/D =0.6, 1 and 1.4 is slightly higher than those obtained with lubricated specimens. So, lubrication should always be used in the dynamic tests to quantify the reliable results.

Figure 46 shows the calculated temperature increase (ΔT) as a function of true plastic strain at different strain rates for both lubricated and unlubricated conditions. It is evident that the rise in temperature of the specimens during adiabatic heating is a little bit higher when friction exists between the specimen and incident-transmitted bars. The ΔT increases with plastic strain for all the strain rates. So, we can conclude that proper lubrication is required between the specimen and pressure bars to avoid potential errors during dynamic testing.

The experimental results obtained from the specimens of different diameters show that the aluminum alloy AA7050-T351 is not sensitive to strain rate below 1000 s^{-1}. The yield stress measured at different strain rates ranging from 400 s^{-1} – 1000 s^{-1} is nearly the same (Figures 39-41). The yield stress increases as the strain rates are increased above 1000 s^{-1} (Figure 38) which means that the strain rate sensitivity of AA7050-T351 is similar to other conventional aluminum alloys as described already in section 1.5. The strain rate sensitivity increases at high strain rates because of the change in mechanism controlling the plastic deformation. At lower strain rates, plastic deformation is governed by the thermally activated dislocation motion and at the strain rates above 1000 s^{-1}, the mechanism changes to dissipative drag mechanisms [28,30-32].

The bigger specimens and larger aspect ratios will bring difficulties in testing and the results. If the specimen is bigger, the size of the incident and transmitted bars should be made even larger to satisfy the one-dimensional stress state. Moreover, the longer specimens will invite the problems of buckling and high inertia effects. So, from the experiments conducted in this work, it is recommended to use the specimens with diameters between 5mm-10 mm with lubrication between the specimen and pressure bars and the most appropriate length to diameter ratio is between 0.6 to 1.4. Considering the specimen buckling and the inertial effects, the aspect ratio of 1 should be used for moderate-high strain rates and an aspect ratio of 0.6 for very high strain rates. Similar recommendations are also given in [61]. Also, the compatibility of cuboid and cylindrical specimens were studied in Figure 48. The cuboid specimens in the compression tests should always be discarded as the deformation is not uniform and high-level stresses are concentrated only on the corners of the cuboid specimens [53].

The JC-model parameters were derived by fitting the experimental stress-strain curves and those parameters were also used in the numerical simulations. Also, the detailed study of friction effects in the dynamic tests was studied using finite element simulations. The simulations were conducted using the different dynamic coefficients of friction, μ = 0, 0.1, 0.2, 0.3, 0.4 and 0.5. The results are shown in Figure 54 and it clearly demonstrates that the reflected wave decreases slightly with an increase in friction between the specimen and the pressure bars whereas the transmitted wave increases significantly. Figures 55-60 compare the experimental results, JC-model curve and the simulated curves plotted using different coefficients of friction. The simulation results also show that the measured strength increases with an increase in friction. The simulated elastic part of the curve obtained with $\mu = 0$ matches the experimental curves but there is some deviation in the simulated plastic curves. Simulated stress-strain curves with higher friction only matched the experimental results. The most accurate simulated results, when compared with the experimental results, were obtained using the length to diameter ratio of 0.6 and 1.4 in all the cases.

6. CONCLUSIONS AND FUTURE WORK

6.1 Conclusions

Finite element simulations and high strain rate compression tests were conducted using lubricated and unlubricated specimens of AA 7075-T351 with various diameters and aspect ratios. Cylindrical and cuboid specimens were used in the experiments and simulations were carried out using 2D-axisymmetric finite element models. Following conclusions can be drawn from this work:

- The tested alloy shows a low strain rate sensitivity at room temperature.
- Higher strain rates can be achieved with a smaller diameter and shorter specimen. Also, the specimen with short aspect ratio, L/D =0.6 is sensitive to lubrication but not the longer specimens, L/D =1 and 1.4.
- Lubrication should be used to reduce interfacial friction between the incident/transmitted bars and specimen and reduce the errors.
- The appropriate specimens are with diameters between 5mm-10 mm and length to diameter ratios of 0.6-1.4 with the lubrication between the specimens and pressure bars. Besides friction, inertial effects and specimen buckling may also influence the characterization of dynamic mechanical behavior. So, with these considerations, the aspect ratio of 1 should be used for moderate-high strain rates and an aspect ratio of 0.6 for very high strain rates.
- Cuboid specimens should be discarded for high strain rate compression tests.
- Johnson-Cook model parameters were obtained by fitting the experimental stress-strain results and those parameters were used in the numerical simulations. The simulations performed with different coefficients of friction showed that the reflected wave decreases slightly with an increase in friction whereas the transmitted wave increases significantly. The simulation results with only higher friction coefficients matched the experimental results.

6.2 Future work

The work done in this thesis provided some understanding of the importance of using lubrication between the pressure bars and specimen and to select the accurate specimen

diameter and aspect ratio at high strain rates. Following works should be studied in future:

- A better study of the mechanical behavior of AA 7050-T351 at different strain rates up to failure. Also, perform the high strain rates at different temperatures and understand the effects of temperature on mechanical behavior.
- Obtain better JC-model parameters by performing the dynamic tests at higher temperatures to get the value of m and calculating the value of yield stress at quasi-static tests. Also, perform the numerical simulations again to check if better results could be obtained.
- Include damage and fracture criterion in the JC- model to study the failure strain of the alloy at different strain rates.
- Carry out the numerical simulations using the 3D model and check the accuracy of the results obtained with a 2D-model.

REFERENCES

[1] R.M. Davies, A Simple Modification of the Hopkinson Pressure Bar, Proc. 7th Int. Cong. on Applied Mechanics, Vol. 1,1948, pp.404.

[2] Kolsky H., An Investigation of the Mechanical Properties of Materials at Very High Rates of Loading, Proceedings of the Physical Society of Great Britain Series B, Vol. 62,1949, pp.676-700.

[3] Anderson K., John W, J. Gilbert Kaufman, ASM Handbook, Volume 2B, Properties and Selection of Aluminum Alloys, pp.466-506.

[4] Al-Rubaie K.S., Grande M.A.D., Travessa D.N., Cardoso K.N., Effect of pre-strain on the fatigue life of 7050-T7451 Aluminum alloy, Materials Science and Engineering A 464, 2007, pp.141–150.

[5] I.W. Hall, M. Guden, Split Hopkinson Pressure Bar compression testing of an aluminum alloy: Effect of lubricant type, Journal of Materials Science Letters 22, 2003, pp.1533-1535.

[6] Blaz L., E. Evangelista, Strain rate sensitivity of hot deformed Al and AlMgSi alloy. Materials Science and Engineering A207,1996, pp.195- 201.

[7] Meyers M.A., Dynamic Behavior of Materials, John Willey & Sons,1994.

[8] Yu T.X., Xin M.Q., Introduction of impact dynamics, John Wiley & Sons Singapore Pt. Ltd, 2018.

[9] Tim Svensson, Filip Tell, Stress Wave Propagation Between Different Materials, Chalmers University of Technology, Master's thesis, 2015.

[10] H. Kuhn, D. Medlin. ASM Handbook, Volume 8: Mechanical Testing and Evaluation, pp.427–428.

[11] Hopkinson J. 1901 Further experiments on the rupture of iron wire (1872). In Original papers by the late John Hopkinson, vol. II (ed. B Hopkinson), article 39, pp. 321–324. Cambridge, UK: Cambridge University Press.

[12] B. Hopkinson, The Effects of Momentary Stresses in Metals, Proceedings of the Royal Society of London Series A, Vol. 74, 1905, pp.498.

[13] Hopkinson B., A Method of Measuring the Pressure Produced in the Detonation of High Explosives or by the Impact of Bullets, Proceedings of the Royal Society of London Series A, Vol. 213, 1914, pp.437-456.

[14] R.M. Davies, A Simple Modification of the Hopkinson Pressure Bar, Proc. 7th Int. Cong. on Applied Mechanics, Vol. 1,1948, pp.404.

[15] Kolsky H., An Investigation of the Mechanical Properties of Materials at Very High Rates of Loading. Proceedings of the Royal Society of London, London, B62, 1949, pp.676-700.

[16] H. Kuhn, D. Medlin, ASM Handbook, Volume 8: Mechanical Testing and Evaluation, pp.462–476.

[17] Lindholm U.S., Dynamic Deformation of Metals Under Dynamic Loading, Huffington, N.J. (Ed.), ASME, 1965, pp.42-61.

[18] Lindholm U.S., Yeakley L.M., High strain-rate testing: Tension and compression, Experimental Mechanics, Vol. 8, Issue 1, 1968, pp.1-9.

[19] Follansbee P.S., Frantz C., Wave Propagation in the Split Hopkinson Pressure Bar. Journal of Engineering Materials and Technology, Vol. 105, No. 1,1983, pp. 61-66.

[20] Lindholm U.S., Yeakley L.M., High Strain Rate Testing: Tension and Compression, Exp. Mech., Vol. 8, 1968, pp.1–9.

[21] S. Ellwood, L.J. Griffiths D.J. Parry, A Tensile Technique for Materials Testing at High Strain Rates, Journal of Physics E, Science Instrumentation, Vol. 15,1982, pp.1169–1172.

[22] T. Nicholas, Tensile Testing of Materials at High Rates of Strain, Experimental Mechanics, Vol. 21, 1981, pp.177–185.

[23] Wen-Hui L., Zhen-Tao HE., Yu-Qiang C., Si-Wen T., Dynamic mechanical properties and constitutive equations of 2519A aluminum alloy, Trans. Nonferrous Met. Soc. China 24,2014, pp.2179−2186.

[24] Singh N.K., Cadoni E., Singha M.K., Gupta N.K., Dynamic tensile and compressive behaviors of mild steel at a wide range of strain rates, J. Eng Mech., 139(9),2013, pp.1197–1206.

[25] W. Zhou, K. Wu, L. Zhong, C. Zhang, T. Hou, R. D. K. Misra, A Comparative Study on the Dynamic Tensile Behavior of Nanostructured Bainitic and Quenched-Tempered Martensitic Steels, Metals 2018, 8, 728.

[26] Clifton R.J., Dynamic plasticity. Journal of Applied Mechanics, 50, 1983,941–952.

[27] J. D. Campbell, W. G. Ferguson, The temperature and strain rate dependence of the shear strength of mild steel, The Philosophical Magazine: A Journal of Theoretical Experimental and Applied Physics, 21:169, 1970, pp.63-82.

[28] Regazzoni G., Kocks U.F., Follansbee P.S., Dislocation kinetics at high strain rates, Acta Metallurgica, Volume 35, Issue 12, December 1987, pp. 2865-2875.

[29] Follansbee P.S., G. Regazzoni, U. F. Kocks, Mechanical Properties of Materials at High Rates of Strain, Inst. Phys. Conf. Ser. 70, Institute of Physics, London,1984, pp.71.

[30] E. El-Magd, Mechanical properties at high strain rates,Journal de Physique IV Colloque, 1994, 04(C8), pp.C8-149-C8-170.

[31] Kumar A, Hauser F. E, Dorn J.E., Viscous drag on dislocations in aluminum at high strain rates, Acta Metallurgica, vol.16, Sept. 1968.

[32] Weertman J., Vreeland T., Jassby K.M., Dislocation Mechanics at High Strain Rates. In: Rohde R.W., Butcher B.M., Holland J.R., Karnes C.H. (eds) Metallurgical Effects at High Strain Rates. Springer, Boston, MA, 1973.

[33] Follansbee P.S., High-Strain-Rate Deformation of FCC Metals and Alloys, international conference on metallurgical applications of a shock wave and high strain-rate phenomena, Portland, OR, USA, 28 Jul 1985.

[34] D.Hull, D.J. Bacon, Introduction to dislocations, 5th edition. Burlington, MA 01803, USA,2011.

[35] H.Conrad. Thermally activated deformation of metals, Journal of metals-58, July 1964.

[36] Tanaka K., Nojima T., Strain rate change tests of aluminum alloys under high strain rate, In Proceedings of the 19th Japan congress on materials research,1975, Tokyo, Japan, pp. 48-51.

[37] Oosterkamp, L. Djapic, Ivankovic A., Venizelos G., High Strain Rate Properties of Selected Aluminum Alloys, Materials Science & Engineering A, Vol.278, Feb.2000, pp.225-235.

[38] El-Magd.E, Abouridouane, M., Influence of Strain Rate and Temperature on the Compressive Ductility of Al, Mg and Ti Alloys, Journal de Physique IV France, Vol. 110, 2003, pp.15-25.

[39] Mishra B., Mondal C., Goyal R., Ghosal P., K. Siva Kumar, V. Madhu, Plastic flow behavior of 7017and 7055 aluminum alloys under different high strain rate test methods. Materials Science & Engineering, A 612. 2014, pp.343–353.

[40] Lindholm U.S., Bessey R.L., Smith G.V., Effect of Strain Rate on Yield Strength, Tensile Strength, and Elongation of Three Aluminum Alloys, Journal of Materials, Vol. 6, No. 1, 1971, pp.119-133.

[41] J. May, H.W. Höppel, M. Göken, Strain rate sensitivity of ultrafine-grained aluminum processed by severe plastic deformation, Scripta Materialia 53,2005, pp.189–194.

[42] A.V. Priftaj, A.Böhner, J. May, H.W. Höppel, M.Göken, Strain rate sensitivity of ultrafine-grained aluminum alloy AA6061, Materials Science Forum Vols. 584-586, 2008, pp.741-747.

[43] Johnson G. R., Cook W. H., A constitutive model and data for metals subjected to large strains, high strain rates, and high temperatures. Proc. 7th Int. Symp. on Ballistics, Hague, Netherlands, April 1983.

[44] R.W. Klopp, R. J. Clifton, T. G. Shawki, Mech. Mat., 4, 375, 1985.

[45] Akhtar S. Khan, Haowen Liu, Variable strain rate sensitivity in an aluminum alloy: Response and constitutive modeling, International Journal of Plasticity 36, 2012, pp.1–14.

[46] Frank J. Zerilli, Ronald W. Armstrong, Dislocation mechanics based constitutive relations for material dynamics calculations, J. Appl. Phys. 61, 1816 ,1987.

[47] Frank J. Zerilli. Dislocation Mechanics–Based Constitutive Equations, Metallurgical and materials transactions, 2548, Vol 35A, 2004.

[48] P.S. Follansbee, U.F. Kocks, A constitutive description of the deformation of copper-based on the use of the mechanical threshold stress as an internal state variable. Acta Metallurgical, Volume 36, Issue 1, January 1988, pp.81-93.

[49] S. R. Bodner, Y. Partom, Constitutive Equations for Elastic-Viscoplastic Strain-Hardening Materials. J. Appl. Mech. Jun 1975, 42(2),pp.385-389.

[50] Rule W.K., Jones S.E., A Revised Form for the Johnson-Cook Strength Model, International Journal of Impact Engineering, Vol. 21, No. 8, 1998, pp.609-624.

[51] Chen G., C. Ren, Zhihong Ke, Jun Li, Xi. Yang, Modeling of flow behavior for 7050-T7451 aluminum alloy considering microstructural evolution over a wide range of strain rates, Mechanics of Materials 95, 2016, pp.146–157.

[52] J.Q.Tan, Mei Zhan, Shuai Liu, T.Huang, Jing Guo, He Yang, A modified Johnson-Cook model for tensile flow behaviors of 7050-T7451aluminum alloy at high strain rates, Materials Science & Engineering A 631,2015, pp.214–219.

[53] Zhong W.Z., Rusinek A., Jankowiak T., Abed F., Bernier R., Sutter G., Influence of interfacial friction and specimen configuration in the Split Hopkinson Pressure Bar system. Tribol Int. 2015.

[54] E. Siebel, Stahl u. Eisen 43,1923,1295.

[55] E.D. H. Davies, S.C.Hunter, The dynamic compression testing of solids by the method of the split Hopkinson pressure bar, J. Mech. Phys. Solids, 1963. Vol.11, pp.115-179.

[56] D. Gorham, An effect of specimen size in the high strain rate compression test, Journal de Physique IV Colloque, 01 (C3), pp.C3-411-C3-418,1991.

[57] Nobuhiko K., Takeshi I., Alexis R., A Study on Reduction of Friction in Impact Compressive Test Based on The Split Hopkinson Pressure Bar Method by Using a Hollow Specimen, Applied Mechanics and Materials Vol. 566, 2014, pp. 548-553.

[58] K. Wang, N.Bahlouli, R. Matadai Boumbimba, F.Addiego, Specimen Geometry Effect on the Deformation Mechanisms of Polypropylene-Based Composites Under Impact Loading at Different Temperatures, J. dynamic behavior, 2016, pp.101–111.

[59] Meyer L. W., Herzig N., Krüger L., Size effects on flow stress and failure of Ti-6-22-22S and Al7075 over a wide range of strain rates. Proc., 11th Int. Conf. on Fracture, Turin, Italy, 2005.

[60] Yokoyama T., Mayama T., Effect of specimen geometry on dynamic compressive stress-strain relations in the case of SHB technique, Oryoku. Hizumi Sokutei to Kyodo Hyoka Shinpojiumu Koen Ronbunshu, 34, 2003, pp.67–72.

[61] Iram Raza Ahmad, Dong Wei Shu, Effect of Specimen Diameter in Compression at High Strain Rates, Journal of Engineering Mechanics, Vol. 137, No. 3, March 1, 2011.

[62] P. Li, C.R. Siviour, N. Petrinic, The Effect of Strain Rate, Specimen Geometry and Lubrication on Responses of Aluminium AA2024 in Uniaxial Compression Experiments, Experimental Mechanics 49, 2009, pp.587–593.

[63] Hallquist J., LS-DYNA Theoretical Manual, Livermore software technology corporation,1998.

[64] Luo J., Li M.Q., Wu B., The correlation between flow behavior and microstructural evolution of 7050 aluminum alloy, Materials Science and Engineering A 530, 2011, pp.559‑564.

[65] Jin Q.A., Mei Z., Liu S., Huang T., Jing G., Yang He., A modified Johnson-Cook model for tensile flow behaviors of the 7050-T7451 aluminum alloy at high strain rates, Materials Science & Engineering A, 631, 2015, pp.214–219.

[66] H.E. Hu, L. Zhen, B.Y. Zhang, L. Yang, J.Z. Chen, Microstructure characterization of 7050 aluminum alloy during dynamic recrystallization and dynamic recovery, Materials characterization 59, 2008, pp.1185 – 1189.

[67] J. J. Mason, A. J. Rosakis, G. Ravichandran, On the strain and strain rate dependence of the fraction of plastic work converted to heat: an experimental study using high-speed infrared detectors and the Kolsky bar, Mech. Mater., vol. 17, 1994, pp. 135–145.

[68] D. Rittel, L. H. Zhang, S. Osovski, The dependence of the Taylor–Quinney 87 coefficient on the dynamic loading mode, J. Mech. Phys. Solids, vol. 107, 2017, pp. 96– 114.

[69] Rouse, J.P., Hyde, C.J. Kazakeviciute J., Investigations into Taylor-Quinney coefficient determination for a 7000 series aluminum alloy using a novel small specimen test technique, Ubiquity Proceedings, 2018.

[70] Y. N. Li, D. G. Karr, G. Wang, Mesh Size Effects in Simulating Ductile Fracture of Metals, 10th International Symposium on Practical Design of Ships and Other Floating Structures,2007.

[71] Jin W.N, Jang-Ho J.K., Sung B. K., Na H.Y., Keun J.B., A Study on Mesh Size Dependency of Finite Element Blast Structural Analysis Induced by Non-uniform Pressure Distribution from High Explosive Blast Wave, KSCE Journal of Civil Engineering, 2008, pp.259-265.

[72] Goran L., Martin F., Ragnar L., Rate Sensitive Continuum Damage Models and mesh Dependence in Finite Element Analyses, Hindawi Publishing Corporation, 2014.